



1 **ModIs Dust AeroSol (MIDAS): A global fine resolution dust optical depth dataset**

2

3 Antonis Gkikas¹, Emmanouil Proestakis¹, Vassilis Amiridis¹, Stelios Kazadzis^{2,3}, Enza Di Tomaso⁴,
4 Alexandra Tsekeri¹, Eleni Marinou⁵, Nikos Hatzianastassiou⁶ and Carlos Pérez García-Pando^{4,7}

5

6 ¹Institute for Astronomy, Astrophysics, Space Applications and Remote Sensing, National Observatory of Athens,
7 Athens, 15236, Greece

8 ²Physikalisch-Meteorologisches Observatorium Davos, World Radiation Center, Switzerland

9 ³Institute of Environmental Research and Sustainable Development, National Observatory of Athens, Greece

10 ⁴Earth Sciences Department, Barcelona Supercomputing Center, Barcelona, Spain

11 ⁵Deutsches Zentrum für Luft- und Raumfahrt (DLR), Institut für Physik der Atmosphäre, Oberpfaffenhofen, Germany

12 ⁶Laboratory of Meteorology, Department of Physics, University of Ioannina, Ioannina, Greece

13 ⁷ICREA, Passeig Lluís Companys 23, 08010 Barcelona, Spain

14

15

16 Corresponding author: Antonis Gkikas (agkikas@noa.gr)

17

18 **Abstract**

19 Monitoring and describing the spatiotemporal variability of dust aerosols is crucial to understand
20 their multiple effects, related feedbacks and impacts within the Earth system. This study describes
21 the development of the MIDAS (ModIs Dust AeroSol) dataset. MIDAS provides columnar daily dust
22 optical depth (DOD at 550 nm) at global scale and fine spatial resolution (0.1° x 0.1°) over a decade
23 (2007-2016). This new dataset combines quality filtered satellite aerosol optical depth (AOD)
24 retrievals from MODIS-Aqua at swath level (Collection 6, Level 2), along with DOD-to-AOD ratios
25 provided by MERRA-2 reanalysis to derive DOD on the MODIS native grid. The uncertainties of
26 MODIS AOD and MERRA-2 dust fraction with respect to AERONET and CALIOP, respectively,
27 are taken into account for the estimation of the total DOD uncertainty (including measurement and
28 sampling uncertainties). MERRA-2 dust fractions are in very good agreement with CALIOP column-
29 integrated dust fractions across the “dust belt”, in the Tropical Atlantic Ocean and the Arabian Sea;
30 the agreement degrades in North America and the Southern Hemisphere where dust sources are
31 smaller. MIDAS, MERRA-2 and CALIOP DODs strongly agree when it comes to annual and
32 seasonal spatial patterns; however, deviations of dust loads’ intensity are evident and regionally
33 dependent. Overall, MIDAS is well correlated with ground-truth AERONET-derived DODs
34 (R=0.882), only showing a small negative bias (-0.009 or -5.307%). Among the major dust areas of
35 the planet, the highest R values (up to 0.977) are found at sites of N. Africa, Middle East and Asia.



36 MIDAS expands, complements and upgrades existing observational capabilities of dust aerosols and
37 it is suitable for dust climatological studies, model evaluation and data assimilation.

38

39 **1. Introduction**

40 Among tropospheric and stratospheric aerosol species, dust aerosol is the most abundant
41 component in terms of mass, contributing more than half to the global aerosol amount (Textor et al.,
42 2006; Zender et al., 2011). Preferential sources of dust aerosol are located in areas where precipitation
43 is low, thus favoring aridity, whereas a significant contributing factor is the accumulation of alluvial
44 sediments. Such regions comprise deserts, dry lake beds and ephemeral channels (e.g., Middleton and
45 Goudie, 2001; Prospero et al., 2002; Ginoux et al., 2012). Previous studies (Prospero et al., 2002;
46 Ginoux et al., 2012), have shown that the major portion of the global dust burden originates from the
47 Sahara Desert, which hosts the most intense dust source of the planet, the Bodélé Depression located
48 in the northern Lake Chad Basin. In North Africa, large amounts of mineral particles are also emitted
49 in the Western Sahara while other noticeable sources of smaller spatial extension are located in the
50 eastern Libyan Desert, in the Nubian Desert (Egypt) and Sudan (Engelstaedter et al., 2006).

51 One of the major dust sources of the planet, following N. Africa, is the Middle East with several
52 active regions (Pease et al., 1998; Hamidi et al., 2013; Yu et al., 2013) in which wind-blown dust is
53 emitted from alluvial plains (Tigris-Euphrates River) and sandy deserts (Rub al Khali Desert).
54 Important dust sources are also recorded in the Asian continent, particularly in the Taklamakan Desert
55 (Ge et al., 2014), in the Gobbi Desert (Chen et al., 2017), in its central parts (Karakum Desert; Li and
56 Sokolik, 2018), in the Sistan Basin (Alizadeh Choobari et al., 2013) and in desert areas (e.g. Thar
57 Desert) situated in the Indus valley plains of Pakistan (Hussain et al., 2005). In North America,
58 mineral particles emitted from the Mojave and Sonoran deserts (Hand et al., 2017) have mainly
59 natural origin while in the Chihuahuan Desert as well as in the Southern Great Plains the
60 anthropogenic interference on soil can favor emission of dust particles and subsequently their
61 entrainment in the atmosphere (Hand et al., 2016). Overall, the major portion of the global dust budget
62 arises from the deserts of the N. Hemisphere (Ginoux et al., 2012) while mineral aerosols are also
63 emitted in Australia (Ekström et al., 2004), South Africa (Bryant et al., 2007; Vickery et al., 2013)
64 and South America (Gassó and Torres, 2019), but to a lesser extent. At global scale, most of the
65 entrained dust loads in the atmosphere originate from tropical and sub-tropical arid regions; however,
66 about 5% of the global dust budget consists of particles emitted from high-latitude sources (Bullard
67 et al., 2016).



68 Dust plays a key role in several aspects of the Earth system such as climate (e.g. Lambert et al.,
69 2013; Nabat et al., 2015) and weather (Pérez et al., 2006; Gkikas et al., 2018; Gkikas et al., 2019),
70 attributed to the perturbation of the Earth-Atmosphere system radiation budget (Sokolik and Toon,
71 1996; Haywood and Bucher, 2000) by mineral particles, the productivity of oceanic waters (Jickells
72 et al., 2005) and terrestrial ecosystems (Okin et al., 2004), and humans' health (Kanatani et al., 2010;
73 Kanakidou et al., 2011; Pérez García-Pando et al., 2014; Du et al., 2016). Dust is characterized by a
74 pronounced temporal and spatial variability due to the heterogeneity of the emission, transport and
75 deposition processes governing the dust life cycle (Schepanski, 2018). A variety of atmospheric
76 circulation mechanisms, spanning from local to planetary scales, are responsible for the uplifting of
77 erodible particles from bare soils (Koch and Renno, 2005; Knippertz et al., 2007; Klose and Shao,
78 2012; Fiedler et al., 2013) and their subsequent transport (Husar et al., 2001; Prospero and Mayol-
79 Bracero, 2013; Yu et al., 2015; Flaounas et al., 2015; Gkikas et al., 2015), accumulation and removal
80 (Zender et al., 2003; Ginoux et al., 2004) from the atmosphere.

81 Given the scientific importance of dust in the Earth system as well as the numerous socioeconomic
82 impacts (Stefanski and Sivakumar, 2009; Weinzierl et al., 2012; Kosmopoulos et al., 2018), there is
83 a need to monitor and forecast dust loads at different spatiotemporal scales. Contemporary satellite
84 observations, available over long-term periods, have been proven a powerful tool in such efforts as
85 they provide wide spatial coverage, relatively high sampling frequency and considerably high
86 accuracy. Spaceborne retrievals have been widely applied in aerosol research for the description of
87 dust loads' features and their evolution (e.g., Kaufman et al., 2005; Liu et al., 2008; Peyridieu et al.,
88 2013; Rashki et al., 2015; Gkikas et al., 2013; 2016; Marinou et al., 2017; Proestakis et al., 2018).
89 Even more accurate aerosol observations, but locally restricted, are derived by ground-based
90 platforms consisting of sunphotometers, lidars and in-situ instruments. Based on these measurements,
91 columnar optical and microphysical properties of mineral particles have been analyzed extensively
92 (Giles et al., 2012), altitude-resolved information of optical properties has provided insight about the
93 dust vertical distribution (Mamouri and Ansmann, 2014), and a comprehensive description of dust
94 optical, microphysical and chemical properties has been achieved from surface and aircraft in-situ
95 instruments (Rodríguez et al., 2012; Liu et al., 2018). Finally, through the deployment of atmospheric-
96 dust models (e.g., Pérez et al., 2011; Haustein et al., 2012), global (e.g., Ginoux et al., 2004) and
97 regional (e.g., Basart et al., 2012) displays of dust burden have been realized.

98 Traditionally, observations have been utilized to evaluate and eventually constrain model
99 performance. Observations are increasingly used in data assimilation (DA) schemes for aerosol
100 forecast initialization (Di Tomasso et al., 2017) and development of reanalysis datasets (Benedetti et
101 al., 2009; Lynch et al., 2016; Gelaro et al., 2017). The most exploited reanalysis datasets in dust-



102 related studies, are the MERRAero (Modern Era Retrospective analysis for Research and
103 Applications Aerosol Reanalysis; Bucharth et al., 2015) and its evolution MERRA-2 (Modern-Era
104 Retrospective analysis for Research and Applications, Version 2; Gelaro et al., 2017) as well as
105 CAMSRA (Copernicus Atmosphere Monitoring Service Reanalysis; Innes et al., 2019) and its
106 predecessor MACC (Monitoring Atmospheric Composition and Climate; Inness et al., 2013). Current
107 reanalysis datasets provide information about dust aerosols at high temporal resolution and decadal
108 time scales. However, even though aerosol optical depth (AOD) observations are assimilated, the
109 performance of the simulated outputs is partly model-driven and their resolution is relatively coarse.

110 The overarching goal of the present study is to describe the development of the MIDAS (ModIs
111 Dust AeroSol) dataset, which provides dust optical depth (DOD) over a decade (2007-2016). The
112 powerful element of this product is its availability at fine spatial resolution ($0.1^\circ \times 0.1^\circ$) as well as
113 the provision of full global coverage, i.e. both over land and ocean. Ginoux et al. (2012) analyzed
114 DOD at the same spatial resolution and for a long-term period but they restricted only above
115 continental surfaces since their scientific focus was the identification of natural and anthropogenic
116 dust sources. Voss and Evan (2020) combined satellite (MODIS, AVHRR) aerosol retrievals and
117 MERRA-2 winds, and analyzed DOD over long-term periods at coarse spatial resolution ($1^\circ \times 1^\circ$).
118 Vertical dust (and other aerosol) backscatter and extinction profiles along with the respective column
119 integrated AODs at $1^\circ \times 1^\circ$ spatial resolution are distributed through the LIVAS database (Amiridis
120 et al., 2015). Therefore, the developed MIDAS dataset expands, complements and upgrades existing
121 observational capabilities of dust aerosols being suitable for research studies related to climatology,
122 model evaluation and data assimilation.

123 For the development of the fine resolution MIDAS DOD, a synergy of MODIS-Aqua (Section
124 2.1), MERRA-2 (Section 2.2), CALIPSO-CALIOP (Section 2.3) and AERONET (Section 2.4)
125 aerosol products has been deployed by taking advantage of the strong capabilities of each dataset.
126 Based on the applied methodology (Section 3.1), the DOD is calculated by the product of MODIS-
127 Aqua Level 2 AOD and the collocated DOD-to-AOD ratio from MERRA-2. The uncertainty of the
128 DOD is calculated from the uncertainties of both MODIS AOD and the MERRA-2 dust fraction,
129 using AERONET and CALIOP, respectively, as a reference (Section 3.2). We thoroughly compare
130 the MERRA-2 dust fraction against the CALIOP dust portion in Section 4.2. The MIDAS DOD is
131 evaluated against AERONET in Section 4.3 and compared with MERRA-2 and CALIOP DODs in
132 Section 4.4. In section 4.5 we provide the annual and seasonal global geographical distributions of
133 DOD. Finally, the main findings are summarized and are drawn in Section 5.

134



135 **2. Datasets**

136 *2.1. MODIS*

137

138 The MODerate resolution Imaging Spectroradiometer (MODIS) is a passive sensor measuring
139 the top of atmosphere (TOA) reflectance in order to retrieve aerosol optical depth (AOD), among
140 other aerosol optical properties, at various wavelengths spanning from the visible to the near infrared
141 spectrum range. MODIS is mounted on the NASA's twin polar satellites Terra and Aqua acquiring
142 high-quality aerosol data since 2000 and 2002, respectively, while thanks to its wide swath (~2330
143 km) provides near-global observations, almost on a daily basis. The derivation of AOD is achieved
144 through the implementation of three retrieval algorithms based on the Dark Target (DT) approach,
145 valid over oceans (Remer et al., 2002; 2005; 2008) and vegetated continental areas (Levy et al., 2007a;
146 2007b; 2010), or the Deep Blue (DB) approach (Hsu et al., 2004; Sayer et al., 2013) over land surfaces
147 characterized by high reflectivity. Depending on the version of the retrieval algorithms, the MODIS
148 datasets are organized at various collections as well as at various levels corresponding to their spatial
149 and temporal resolution. For our purposes, we are utilizing the Collection 6 (C006) MODIS-Aqua
150 Level 2 (L2) retrievals, over the period 2007-2016, which are reported at 5-min swath granules (Levy
151 et al., 2013) and are accessible from the Level-1 and Atmosphere Archive & Distribution System
152 (LAADS) Distributed Active Archive Center (DAAC) (<https://ladsweb.modaps.eosdis.nasa.gov/>).
153 Each swath is composed by 203 x 135 retrievals, of increasing spatial resolution from the nadir view
154 (10 km x 10 km) towards the edge of the satellite scan (48 km x 20 km), in which a Quality Assurance
155 (QA) flag is assigned (Hubanks, 2018). More specifically, these bit values represent the reliability of
156 the algorithm output and are equal to 0 ("No Confidence"), 1 ("Marginal"), 2 ("Good") and 3 ("Very
157 Good"). As it has been mentioned above, the MODIS AOD retrievals are acquired based on different
158 algorithms according to the underlying surface type. In order to fill observational gaps, attributed to
159 the assumptions or limitations of the applied MODIS algorithms, the DT-Ocean ($QA \geq 1$), DT-Land
160 ($QA = 3$) and DB-Land ($QA \geq 2$) AOD retrievals are merged based on the Normalized Difference
161 Vegetation Index (NDVI) and the highest accuracy criterion, as it has been presented by Sayer et al
162 (2014). From the raw MODIS files, this "merged" AOD stored in the scientific data set (SDS) and
163 named "AOD_550_Dark_Target_Deep_Blue_Combined" is extracted and processed for the needs of
164 the current work. Finally, two quality filtering criteria are applied to the raw MODIS AODs for
165 eliminating observations which may be unreliable. AODs associated with cloud fraction (CF) higher
166 than 0.8 as well as those with no adjacent retrievals are masked out following the recommendations
167 of previous studies (Anderson et al., 2005; Zhang and Reid, 2006; Hyer et al., 2011; Shi et al., 2011).
168 The first criterion is associated with the potential cloud contamination of AODs, and the second
169 attempts at removing "suspicious" retrievals from the dataset.



170

171 2.2. MERRA-2

172

173 The Modern-Era Retrospective Analysis for Research and Applications, version 2 (MERRA-2),
174 developed by the NASA Global Modeling and Assimilation Office (GMAO), is the first atmospheric
175 reanalysis spanning over the new modern satellite era (1980 onward) in which aerosol-radiation
176 interactions and the two-way feedbacks with atmospheric processes are taken into account (Gelaro et
177 al., 2017). The key components of MERRA-2 (Buchard et al., 2017) are the Goddard Earth Observing
178 System (GEOS-5) (Rienecker et al. 2008; Molod et al. 2015), which is radiatively coupled to the
179 Goddard Chemistry Aerosol Radiation and Transport model (GOCART; Chin et al. 2002; Colarco et
180 al. 2010), and the three-dimensional variational data assimilation (3DVar) Gridpoint Statistical
181 Interpolation analysis system (GSI) (Wu et al. 2002).

182 In the GOCART aerosol module, emission, sinks, removal mechanisms (dry deposition and
183 gravitational settling, large-scale wet removal and convective scavenging) as well as the chemical
184 processes of five aerosol species (dust, sea-salt, sulfate, and black and organic carbon) are simulated.
185 Their optical properties are based on the updated Optical Properties of Aerosols and Clouds (OPAC)
186 database (Hess et al. 1998), incorporating dust non-spherical shape (Meng et al. 2010; Colarco et al.
187 2014), and are calculated according to Colarco et al. (2010). For coarse particles (i.e., dust and sea-
188 salt), five non-interacting size bins are considered whose emissions are driven by the wind speed
189 based on the parameterizations of Marticorena and Bergametti (1995) for dust and the modified
190 version of Gong (2003) for sea-salt. Both hydrophobic and hydrophilic black (BC) and organic (OC)
191 carbon emitted from anthropogenic activities (i.e., fossil fuel combustion) and natural processes (i.e.,
192 biomass burning) are considered. Regarding sulfate aerosols (SO₄), these either are primarily emitted
193 or are formed by the chemical oxidation of sulfur dioxide gas (SO₂) and dimethyl sulfide (DMS).
194 Until 2010, daily emissions of eruptive and degassing volcanoes are derived from the AeroCom Phase
195 II project (Diehl et al. 2012; <http://aerocom.met.no/>) and afterwards only a repeating annual cycle of
196 degassing volcanoes is included in MERRA-2. The hygroscopic growth of sea-salt, sulfate and
197 hydrophilic carbonaceous aerosols is determined by the simulated relative humidity (RH) and the
198 subsequent modification of particles' shape and composition is taken into account in computations of
199 particles' fall velocity and optical parameters (Randles et al., 2017). A detailed description of the
200 emission inventories along with the global climatological maps, representative for the period 2000 –
201 2014, are given in Randles et al. (2017).

202 MERRA-2 is a multidecadal reanalysis in which a variety of meteorological and aerosol
203 observations are jointly assimilated (Gelaro et al., 2017). The former group of observations consists
204 of ground-based and spaceborne atmospheric measurements/retrievals summarized in Table 1 of



205 Gelaro et al. (2017) while the full description is presented in McCarty et al. (2016). For aerosol data
206 assimilation, the core of the utilized satellite data is coming from the MODIS instrument. Over
207 oceans, are also used AVHRR radiances, from January 1980 to August 2002, and over bright surfaces
208 (albedo > 0.15) the non-bias-corrected AOD (February 2000 – June 2014) retrieved for the Multiangle
209 Imaging SpectroRadiometer (MISR; Kahn et al., 2005) is assimilated. Apart from satellite datasets,
210 the Level 2 (L2) quality-assured AERONET retrievals (1999 – October 2014; Holben et al., 1998)
211 are integrated in the MERRA-2 assimilation system (Goddard Aerosol Assimilation System, GAAS)
212 which is presented in Randles et al. (2017; Section 3). From MODIS (above dark target continental
213 and maritime areas, Collection 5) and AVHRR (above oceanic regions), the AODs are retrieved from
214 the cloud-free radiances and adjusted (bias correction) to the corresponding AERONET AODs, via a
215 neural net retrieval (NNR). It must be clarified, that only the MERRA-2 AOD is directly constrained
216 by the observations while the model’s performance (background forecast) and data assimilation
217 structure (parameterization of error covariances) are “responsible” for the aerosol speciation among
218 other aerosol diagnostics (Buchard et al., 2017).

219 In the present study, we use the columnar MERRA-2 total and dust AOD at 550 nm in order to
220 calculate the contribution, in optical terms, of mineral particles to the overall load. The computed
221 dust-to-total AOD ratio is evaluated against CALIOP retrievals and then used for the derivation of
222 dust optical depth (DOD) on MODIS-Aqua swaths. MERRA-2 products (M2T1NXAER files;
223 V5.12.4; aerosol diagnostics) have been downloaded from the GES DISC server
224 (<https://disc.gsfc.nasa.gov/>) and are reported as hourly averages at $0.5^\circ \times 0.625^\circ$ lat-lon spatial
225 resolution.

226

227 2.3. CALIOP

228

229 The Cloud Aerosol Lidar with Orthogonal Polarization (CALIOP), onboard the Cloud-Aerosol
230 Lidar and Infrared Pathfinder Satellite Observation (CALIPSO) satellite, provides altitude resolved
231 observations of aerosols and clouds since mid-June 2006 (Winker et al., 2010). CALIPSO, flying in
232 the A-Train constellation (Stephens et al., 2002), provides almost simultaneous observations with
233 Aqua thus making feasible and powerful their synergistic implementation for aerosol research.
234 CALIOP, an elastic backscatter two-wavelength polarization-sensitive Nd:YAG lidar in a near-nadir-
235 viewing geometry (since November 28, 2007, 3 degrees off-nadir), emits linearly polarized light at
236 532 and 1064 nm and detects the co-polar components at 532 and 1064 nm and the cross-polar
237 component at 532 nm, relative to the laser polarization plane (Hunt et al., 2009). Based on the
238 attenuated backscatter profiles (Level 1B) and the implementation of retrieval algorithms (Winker et
239 al., 2009), aerosol/cloud profiles as well as layer products are provided at various processing levels



240 (Tackett et al., 2018). CALIOP Level 2 (L2) aerosol and cloud products both are provided at a uniform
241 spatial resolution at horizontal (5 km) and vertical (60 m) dimensions. Detectable atmospheric
242 features are first categorized to aerosols or clouds and then are further discriminated at specific
243 subtypes according to Vaughan et al. (2009). For aerosols, in the Version 3 used here, 6 subtypes are
244 considered consisting of clean marine, dust, polluted continental, clean continental, polluted dust and
245 smoke (Omar et al., 2009). Based on the aerosol subtype classification, specific extinction-to-
246 backscatter ratios (Lidar Ratio - LR) are applied for the provision of extinction coefficient profiles
247 along the CALIPSO orbit-track (Young and Vaughan, 2009).

248 In this study we use the CALIOP pure dust product developed in the framework of the ESA-
249 LIVAS (Amiridis et al., 2015) database (<http://lidar.space.noa.gr:8080/livas/>) according to the
250 methodology described in Amiridis et al. (2013) and updated in Marinou et al. (2017). The
251 aforementioned technique relies on the incorporation of aerosol backscatter coefficient profiles and
252 depolarization ratio, providing a strong signal of dust presence due to mineral particles' irregular
253 shape (Freudenthaler et al., 2009; Burton et al., 2015; Mamouri and Ansmann, 2017), allowing the
254 separation of dust component from aerosol mixtures. For our purposes, instead of the raw universal
255 CALIOP dust LR (40 sr; Version 3), we are applying appropriate regionally-dependent LR values
256 (see Figure S1; Marinou et al., 2017; Proestakis et al. 2018 and references within), which are
257 multiplied with the dust backscatter coefficient profiles at 532 nm in order to calculate the
258 corresponding extinction coefficient profiles. After a series of strict quality screening filters (Marinou
259 et al., 2017), the columnar total/dust/non-dust optical depths as well as the DOD-to-AOD ratio over
260 the period 2007 – 2015 are aggregated at $1^\circ \times 1^\circ$ grid cells covering the whole globe. The performance
261 of the pure DOD product has been assessed against AERONET over N. Africa and Europe (Amiridis
262 et al., 2013) revealing a substantial improvement when the abovementioned methodological steps are
263 applied. This has led to a broadening of research studies, such as the assessment of dust outbreaks
264 (Kosmopoulos et al., 2017; Solomos et al., 2018) and phytoplankton growth (Li et al., 2018), the 4D
265 description of mineral loads over long-term periods (Marinou et al., 2017; Proestakis et al., 2018),
266 the evaluation of dust models (Tsikerdekis et al., 2017; Georgoulas et al., 2018; Konsta et al., 2018)
267 and the evaluation of new satellite products (Georgoulas et al., 2016) in which the LIVAS pure DOD
268 product can be utilized.

269

270 2.4. AERONET

271

272 Ground-based observations acquired from the AERONET RObotic NETwork (AERONET; Holben
273 et al., 1998) have been used as reference in order to evaluate the accuracy of the quality assured



274 MODIS AOD as well as of the derived MODIS DOD product. The evaluation analysis has been
275 performed by utilizing the almucantar (inversion) retrievals, providing information for the total
276 aerosol amount (AOD) as well as for other microphysical (e.g., volume size distribution) and optical
277 (e.g., single scattering albedo) properties (Dubovik and King, 2000; Dubovik et al., 2006). In the
278 present study, focus is put on the aerosol optical properties retrieved at four wavelengths (440, 675,
279 870 and 1020 nm) utilizing as inputs spectral AODs and sky (diffuse) radiances. More specifically,
280 we used the Version 2 (V2) AERONET data of AOD (for total and coarse aerosols), Ångström
281 exponent (α) and single scattering albedo (SSA). For the amount (AOD) and size (α) related optical
282 parameters, the quality assured retrievals (i.e., Level 2; L2) are only used whereas for the SSA, the
283 L2 and Level 1.5 (L1.5) observations are merged in order to ensure maximum availability.
284 Unfavourable atmospheric conditions or restrictions on solar geometry result in a reduced amount of
285 inversion outputs with respect to the sun-direct measurements or the Spectral Deconvolution
286 Algorithm (SDA; O'Neill et al., 2003) retrievals. Even though both types of AERONET data provide
287 information about aerosol size (i.e., Ångström exponent) or coarse AOD (i.e., SDA), the optimum
288 approach for identifying dust particles and discriminating them from other coarse particles (i.e., sea-
289 salt) requires the of SSA, along with size optical properties, as it will be discussed in the next
290 paragraph.

291 Through the combination of the selected optical properties we achieved the spectral matching
292 between ground-based and spaceborne observations as well as the determination of DOD on
293 AERONET retrievals. Regarding the first part, the $\alpha_{440-870\text{nm}}$ and $\text{AOD}_{870\text{nm}}$ values are applied in the
294 Ångström formula in order to interpolate the AERONET AOD at a common wavelength (i.e., 550
295 nm) with MODIS. In contrast to the MODIS-AERONET AOD comparison, the corresponding
296 evaluation for DOD requires a special treatment of AERONET retrievals in order to define, as much
297 as possible based on columnar data, conditions where dust particles either only exist or clearly
298 dominate over other aerosol species. The vast majority of previous studies (e.g., Fotiadi et al., 2006;
299 Toledano et al., 2007; Basart et al., 2009) have relied on combining AOD and α for aerosol
300 characterization, associating the presence of mineral particles with low alpha levels and considerable
301 AODs. Here, we are keeping records where the $\alpha_{440-870\text{nm}} \leq 0.75$ and $\text{SSA}_{675\text{nm}} - \text{SSA}_{440\text{nm}} > 0$ without
302 taking into account the aerosol optical depth. The first criterion ensures the predominance of coarse
303 aerosols while the second one serves as an additional filter for discriminating dust from sea-salt
304 particles, taking advantage of the specific spectral signature of SSA (i.e., decreasing absorptivity for
305 increasing wavelengths in the visible spectrum) in pure or rich dust environments (Giles et al., 2012).

306 Then, from the coarse AODs at 440, 675 and 870 nm we calculate the corresponding α , which is
307 applied in order to obtain the AERONET coarse AOD at 550 nm. This constitutes the AERONET-
308 derived DOD assuming that the contribution of fine dust particles (particles with radii less than the



309 inflection point in the volume size distribution) is small. Likewise, through this consideration any
310 potential “contamination” from small-size particles of anthropogenic or natural origin (e.g., biomass
311 burning), which is likely far away from the sources, is tempered or avoided.

312

313 **3. Methods**

314 *3.1. Derivation of dust optical depth on MODIS swaths*

315

316 The core concept of our approach is to derive DOD on MODIS L2 retrievals, provided at fine
317 spatial resolution, via the synergy with the MERRA-2 products. More specifically, the MERRA-2
318 dust fraction (MDF) to total AOD_{550nm} (Eq. 1) is multiplied with the MODIS AOD_{550nm} in order to
319 calculate DOD_{550nm} at swath-level (Eq. 2).

320

$$321 \quad MDF = \frac{AOD_{DUST,MERRA}}{AOD_{TOTAL,MERRA}} \quad (\text{Eq. 1})$$

322

$$323 \quad DOD_{MODIS} = AOD_{MODIS} * MDF \quad (\text{Eq. 2})$$

324

325 To achieve that, the datasets are collocated temporally and spatially. MERRA-2 outputs are
326 provided at coarse spatial resolution (0.5° x 0.625°) in contrast to MODIS-Aqua observations (10 km
327 x 10 km). MODIS swaths are composed by 203 x 135 retrievals and for each one of them we compute
328 the distance from the MERRA-2 grid points, considering the closest hourly time step to MODIS
329 overpass time. Then, the MERRA-2 dust portion is used to calculate the DOD from the AOD on
330 MODIS swath native grid. Our approach avoids on purpose the inclusion of additional optical
331 properties providing information on aerosol size (α) available from MODIS and absorptivity (Aerosol
332 Index) from OMI that are characterized by inherent limitations. Previous evaluation studies (Levy et
333 al., 2013) have shown that size parameters acquired by MODIS are highly uncertain, particularly over
334 land. In addition, since early 2008, the OMI sensor has lost half of its swath due to the “row-anomaly”
335 issue (Torres et al., 2018) thus “hampering” the MODIS-OMI collocation when it is attempted at fine
336 spatial resolution.

337

338 *3.2 Uncertainty estimation*

339

340 As expressed in Eq. 2, the MIDAS DOD results from the product of MODIS AOD and MDF from
341 MERRA-2. The uncertainty of the DOD product ($\Delta(\text{DOD})$) accounts for the corresponding
342 uncertainties of the AOD and the MDF, which are calculated using AERONET and CALIOP,



343 respectively, as a reference. The mathematical expression of the $\Delta(\text{DOD})$, given in Eq. 3, results from
344 the implementation of the product rule on Eq. 2.

345

$$346 \quad \Delta(\text{DOD}) = \Delta(\text{AOD}) * \text{MDF} + \text{AOD} * \Delta(\text{MDF}) \quad (\text{Eq. 3})$$

347 The term $\Delta(\text{AOD})$ in Eq. 3, representing the expected error (EE) confidence envelope in which
348 ~68% of the MODIS-AERONET AOD differences fall within, varies depending on the MODIS
349 aerosol retrieval algorithm applied. MODIS provides AODs above oceans, dark vegetated land areas
350 as well as over surfaces with high reflectivity (excluding snow- and ice-covered regions) based on
351 retrieval techniques relying on different assumptions whereas over transition zones between arid and
352 vegetated continental parts, DT and DB AODs are merged (Sayer et al., 2014).

353 For each retrieval algorithm, we use the linear equations expressing $\Delta(\text{AOD})$ with respect to
354 AERONET AOD documented in the literature, for DT-Ocean (Levy et al., 2013; Eq. 4), DT-Land
355 (Levy et al., 2010; Eq. 5), and DB-Land (Sayer et al., 2013; Eq. 6) AODs. For the merged (DB+DT)
356 land AOD, the error is calculated via the square root of the quadrature sum of the DT-Land and DB-
357 Land uncertainties (Eq. 7). Before proceeding with the calculation of the $\Delta(\text{DOD})$, few key aspects
358 must be highlighted for the sake of clarity. In equations 4 and 5, the AOD uncertainty is defined as a
359 diagnostic error since it is calculated utilizing AERONET as reference. Here, we are using the same
360 equations replacing AERONET AODs with those given by MODIS. This relies on the fact (results
361 not shown here) that their averages are almost unbiased. For the ocean AOD uncertainty, the defined
362 EE margins (Levy et al., 2013) have been modified in order to sustain symmetry by keeping the upper
363 bound (i.e., thus including more than 68% of MODIS-AERONET pairs within the EE). Sayer et al.
364 (2013) estimated the uncertainty of DB AOD by taking into account the geometric air mass factor
365 (AMF) resulting from the sum of the reciprocal cosines of the solar and viewing zenith angles (Eq.
366 6).

367

$$368 \quad \Delta(\text{AOD}_{\text{DT-Ocean}}) = \pm(0.10 * \text{AOD} + 0.04) \quad (\text{Eq. 4})$$

$$369 \quad \Delta(\text{AOD}_{\text{DT-Land}}) = \pm(0.15 * \text{AOD} + 0.05) \quad (\text{Eq. 5})$$

$$370 \quad \Delta(\text{AOD}_{\text{DB-Land}}) = \pm\left(\frac{0.086+0.56*\text{AOD}}{\text{AMF}}\right) \quad (\text{Eq. 6})$$

$$371 \quad \Delta(\text{AOD}_{\text{DTDB-Land}}) = \pm\sqrt{[\Delta(\text{AOD}_{\text{DT-Land}})]^2 + [\Delta(\text{AOD}_{\text{DB-Land}})]^2} \quad (\text{Eq. 7})$$

372

373 The CALIOP DOD-to-AOD ratio is our reference for estimating the uncertainty limits of the
374 MERRA-2 dust fraction (MDF). The analysis is performed at $1^\circ \times 1^\circ$ spatial resolution considering
375 only grid cells in which both MERRA-2 and CALIOP DODs are higher or equal than 0.02. According



376 to this criterion, more than 450000 CALIOP-MERRA2 collocated pairs have been found which are
377 sorted (ascending order) based on MERRA-2 MDF (ranging from 0 to 1) and then are grouped in
378 equal size bins containing 20000 data each sub-sample. For every group, we computed the median
379 MDF (x axis) as well as the 68th percentile of the absolute MERRA-2 – CALIOP dust fraction (y
380 axis) and then we found the best polynomial fit (Eq. 8).

381

$$\Delta(MDF) = \pm(2.282 * MDF^4 - 6.222 * MDF^3 + 4.700 * MDF^2 - 0.969 * MDF + 0.199) \text{ (Eq. 8)}$$

384 Depending on the selected MODIS algorithm, the appropriate combination between AOD (Eqs.
385 4, 5, 6 and 7) and MDF (Eq. 8) uncertainties is applied to calculate the $\Delta(\text{DOD})$ (Eq. 3) on each
386 measurement (i.e., DOD), at each grid cell, throughout the study period. When averaging each grid
387 cell at each considered timescale the uncertainty is obtained by propagating each individual
388 measurement uncertainty, i.e., taking the square root of the sum of the quadratic $\Delta(\text{DOD})$ divided by
389 the number of available measurements. We also estimate the uncertainty of the average due to
390 sampling using the standard error (i.e., the standard deviation divided by the square root of the number
391 of measurements). These two uncertainty quantities are in turn combined into a total uncertainty that
392 is calculated as the square root of their quadratic sum. The obtained findings will be discussed in
393 parallel with the global spatial patterns (Section 4.5) of dust optical depth in order to provide a
394 measure of the reliability of the derived DOD product.

395

396 4. Results

397

398 On the following sections, a series of analyses including an intercomparison between MERRA-2
399 and MODIS AODs (Section 4.1), the evaluation of MDF with respect to CALIOP (Section 4.2), an
400 evaluation of MIDAS DOD versus AERONET observations (Section 4.3) as well as an
401 intercomparison among MIDAS, CALIOP and MERRA-2 DODs (Section 4.4), is presented. All the
402 aforementioned steps are necessary in order to justify the validity of the applied methodology and to
403 understand its limitations. In the last section (4.5), the global annual and seasonal DOD patterns are
404 presented as a demonstration of the MIDAS dataset and the obtained spatiotemporal features are
405 briefly discussed since a climatological study it is the scientific topic of the companion paper.

406

407 4.1. Intercomparison of MERRA-2 and MODIS AODs

408

409 A prior step of our analysis is to investigate the consistency between MODIS-Aqua and MERRA-
410 2 AODs in order to ensure that they are not similar or identical thus making meaningless the



411 implementation of MODIS, which is not providing observations of high sampling frequency (single
412 overpasses) with respect to MERRA-2 products (hourly outputs). For their intercomparison, the
413 satellite and reanalysis datasets were regridded at $1^\circ \times 1^\circ$ spatial resolution and they have been
414 temporally (satellite overpass – timestep) and spatially (grid cell coordinates) collocated. The average
415 global geographical distributions (2007-2016) of the simulated (MERRA-2) and retrieved (MODIS)
416 AODs are illustrated in Figures 1-i and 1-ii, respectively, along with their difference map (Figure 1-
417 iii) and the corresponding frequency histogram of MERRA-2 – MODIS AOD deviations (Figure 1-
418 iv).

419 A visual comparison between the two patterns does not reveal substantial deviations, in terms of
420 spatial characteristics, as indicated by the reproduction of the maximum AODs over major dust (i.e.
421 Sahara), biomass (i.e., Central Africa) and pollution (i.e., E. Asia) sources as well as over areas (i.e.,
422 Sub-Saharan) where very high concentrations of aerosol mixtures are recorded. A good agreement is
423 also apparent over downwind oceanic regions affected by short-to-long range transport of dust
424 (Tropical Atlantic Ocean) or biomass burning (South Atlantic Ocean). However, the difference map
425 (Fig. 1-iii) reveals substantial deviations, particularly over areas in which specific aerosol types
426 dominate. Across N. Africa, the simulated AODs (MERRA-2) are higher (reddish colors) than the
427 observed ones (MODIS), by up to 0.20-0.25, while positive MERRA-MODIS differences are also
428 encountered over other dust abundant areas such as the Taklamakan Desert and the southwestern
429 parts of Asia. On the contrary, higher MODIS than MERRA-2 AODs (bluish colors in Fig. 1-iii) are
430 predominant in central Africa (by up to 0.3) and evident in the Amazon basin (by up to 0.1) as well
431 as in Indonesia. In the latter regions, the columnar aerosol load mainly consists of carbonaceous
432 particles originating from agricultural burning and wildfires taking place from May to October in
433 central Africa (Bond et al., 2013), from landscape fires in the Amazon, with peak activity in August
434 and September (van der Werf et al., 2006) and from extended burned areas (Giglio et al., 2013) in
435 Indonesia, between August and October (Randerson et al., 2012). Negative differences (i.e. higher
436 MODIS AODs) also appear across the Gangetic Basin, where the major black carbon sources of India
437 are located (Paliwal et al., 2016), while the maximum values (exceeding 0.3) are recorded in the
438 heavily populated and industrialized regions of E. Asia (Zhang et al., 2015), emitting absorbing (black
439 carbon) and scattering (sulphate) fine pollution particles. Above oceans, the majority of reanalysis-
440 satellite departures are negligible, except over the tropical and southern Atlantic Ocean affected by
441 dust and biomass aerosol transport, respectively, with negative biases (i.e., lower MERRA-2 AODs)
442 hardly exceeding 0.05 in absolute terms.

443 The underestimated AODs in MERRA-2 over the major sources of biomass aerosols are probably
444 due to the negative increment in the assimilation system (Buchard et al., 2017). In Asia, GOCART
445 as well as the majority of the existing models underestimate the amount of BC aerosols produced by



446 man-made activities (Koch et al., 2009). Moreover, the anthropogenic OC/BC and SO₂ emissions
447 vary on yearly basis but in MERRA-2 are kept the same after 2006 and 2008, respectively (Randles
448 et al., 2017), while there is a lack of nitrate aerosols (Buchard et al., 2017). All the aforementioned
449 reasons could account for the underestimation of MERRA-2 AOD in Asia as already shown by
450 comparisons against AERONET measurements (Sun et al., 2019). Furthermore, the described
451 inherent weaknesses are intensified by the paucity of ground-based AERONET and cloud-free
452 MODIS retrievals thus reducing the availability of assimilated observations. In such cases, as it has
453 been mentioned by Buchard et al. (2017), the performance of MERRA-2 is driven by the underlying
454 forecast model (GEOS-5). Over N. Africa, as well as in other dust rich environments, the positive
455 reanalysis-satellite biases are mainly linked with the overestimation of GOCART dust aerosol
456 amounts, with respect to a variety of spaceborne observations, as it has been discussed by Yu et al.
457 (2010) and Chin et al. (2014). Moreover, over bright surfaces MERRA-2 assimilates uncorrected
458 MISR AODs, which are higher than the corresponding MODIS retrievals, particularly at low AOD
459 conditions, as it has been shown by Banks et al. (2013) and Farahat (2019). From a global and long-
460 term perspective, the positive and negative deviations of an enormous number of pairs span from -
461 0.3 to 0.3 and are almost equally separated around zero resulting in a Gaussian frequency distribution
462 (Fig. 1-iv).

463

464 4.2. Evaluation of MERRA-2 dust portion versus CALIOP retrievals

465

466 The evaluation of the MERRA-2 dust portion (i.e., MDF) is a critical step of our analysis since it
467 is used as the scaling factor of the MODIS AOD for the derivation of DOD. For this reason, the
468 corresponding columnar parameter computed from the quality assured and updated CALIOP profiles
469 (see Section 2.3) is used as reference. It must be highlighted that the only existing evaluation studies
470 of MERRA-2 aerosol products have been performed either for specific aerosol species or limited time
471 periods (Buchard et al., 2017; Veselovskii et al., 2018) showing the ability of MERRA-2 in
472 reproducing the integrated aerosol fields. Nevertheless, the speciation of the suspended particles,
473 which is to a large extent determined by the model physics assumptions (Gelaro et al., 2017), has not
474 been thoroughly evaluated. Therefore, the present analysis will complement and expand further the
475 current works providing insight about the performance of MERRA-2 in terms of discriminating
476 among aerosol types (particularly for dust) and subsequently estimating their contribution to the total
477 atmospheric load.

478 Figure 2 depicts the geographical distributions of the dust-to-total AOD ratio, based on MERRA-
479 2 (i) and CALIOP (ii), averaged over the period 2007 – 2015. The corresponding maps of mean bias,
480 fractional bias (FB), fractional gross error (FGE) and correlation coefficient (R) are given in Figure



481 3. For consistency, we regridded the MERRA-2 data to $1^\circ \times 1^\circ$ spatial resolution and selected the
482 closest output to the CALIOP overpass time. Both datasets provide nighttime observations; however,
483 the analysis has been restricted to sunlight hours only when aerosol retrievals obtained by passive
484 sensors at visible wavelengths are assimilated. At a first glance, the spatial patterns are very similar,
485 particularly in areas where the presence of dust is predominant. Across the “dust belt” (Prospero et
486 al., 2002), the most evident deviations (underestimation of MERRA-2 dust portion by ~ 0.1 or 10%)
487 are recorded in the borders of Afghanistan and Pakistan (Dasht-e Margo and Kharan Deserts) as well
488 as in the Taklamakan Desert (Fig. 3-i). However, from the FB (Fig. 3-ii) and FGE (Fig. 3-iii) maps it
489 is evident that the calculated values in most of the aforementioned regions are close to zero (ideal
490 score) thus indicating a very good performance of MERRA-2. In terms of temporal covariation (Fig.
491 3-iv), moderate R values (~ 0.5) are computed while in the western parts of Sahara the correlation
492 levels are slightly higher than zero. Due to the complex and highly variable nature of the emission
493 processes and therefore the poorer behavior of the model, the correlation tends to be smaller over the
494 main dust sources. In downwind regions of the N. Hemisphere, particularly over the main transport
495 paths (i.e., Atlantic Ocean, Mediterranean, Arabian Sea, E. Asia), correlation substantially increases
496 (up to 0.9). This is further supported by the FB and FGE metrics; which, however, downgrade for
497 increasing distances from the sources due to the reduction of dust contribution to the total aerosol
498 load. An exception is observed for the mean bias along the tropical Atlantic Ocean where the
499 MERRA-2 dust portion is overestimated by up to 10% in its eastern parts in contrast to longitudes
500 westward of 45° W where zero biases or slight underestimations ($\sim 5\%$, Caribbean Sea) are computed.

501 A discrepancy between the CALIOP and MERRA-2 dust portion is found in the Mojave, Sonoran,
502 Chihuahuan desert areas extending between southwestern US and northern Mexico. As shown in
503 Figure 2, the dust contribution in those areas is more widespread and stronger based on spaceborne
504 retrievals in contrast to MERRA-2, which simulates less dust amount over the sources (Mojave
505 Desert) and the surrounding regions. According to the evaluation metrics (Figure 3), the
506 underestimation of MERRA-2 dust contribution to the total aerosol load ranges between 20% to 50%,
507 negative FB (down to -1) and high FGE values (locally exceeding 1) are evident while the correlation
508 levels are low, particularly over Mexico. In the Southern Hemisphere, the deficiency of MERRA-2
509 is pronounced along the western coasts of S. America as well as in the Patagonian and Monte Deserts,
510 both situated in Argentina. Similar results are found in South Africa while in Australia a contrast
511 between its western/eastern and central parts with slight MERRA-2 underestimations and
512 overestimations, up to 20% in absolute terms, respectively, are recorded (Figure 3-i). Nevertheless,
513 the agreement between MERRA-2 and CALIOP in temporal terms is supported by the moderate-to-
514 high R values over the “hotspot” regions (Figure 3-iv). Outside of the main dust-affected regions, an
515 obvious discrepancy is found in the eastern Canada and northeastern Russia where MERRA-2 dust



516 contribution yields very low values (< 20%) in contrast to CALIOP reaching up to 50%. Due to their
517 geographical position, the occurrence of dust loads might not be frequent there but their contribution
518 to the total load can be significant under low AOD conditions, mainly recorded in the region. This
519 indicates a poor representation by MERRA-2; however, it must also be taken into account a potential
520 cloud contamination in the lidar signals.

521 The discrepancies are mainly driven by the partial representation of dust sources in MERRA-2
522 resulting in potentially underestimated dust emission areas and subsequently to lower dust
523 contribution to the total burden. In many areas dust is originated either from natural (arid lands, salt
524 lakes, glacial lakes) or from anthropogenic sources (Ginoux et al., 2012). Nevertheless, dust sources
525 in MERRA-2 are based on Ginoux et al. (2001) accounting mostly for natural dust emission areas.
526 This could partly explain the higher CALIOP dust contribution levels. Interestingly, most of the
527 positive CALIOP-MERRA-2 differences (i.e. bluish colors in Figure 3-i) are recorded in mountainous
528 areas characterized by complex terrain. Due to the variable geomorphology, the enhanced surface
529 returns contaminate the CALIOP signal close to the ground leading to higher columnar AODs and
530 lower contribution by dust loads suspended aloft. In addition, depending on the homogeneity of the
531 atmospheric scene over regions characterized by complex topography, variations in the optical paths
532 of subsequent CALIPSO L2 aerosol profiles considered in the L3 product may result to unrealistic
533 DOD and AOD values. Previous evaluation studies (e.g., Omar et al., 2013) have shown that CALIOP
534 underestimates AOD with respect to ground-based AERONET retrievals, particularly over desert
535 areas (Amiridis et al., 2015), which was attributed primarily to the incorrect assumption of the lidar
536 ratio (S) (Wandinger et al., 2010) and secondarily to the inability of the lidar to detect thin aerosol
537 layers (particularly during daytime conditions due to low signal-to-noise ratio). The former factor is
538 related to aerosol type and for Saharan dust particles the necessary increase of S (from 40 to 58 sr)
539 improved substantially the level of agreement versus AERONET and MODIS (Amiridis et al., 2013).
540 Similar adjustments (increments) on the raw S values, which are highly variable (Müller et al., 2007;
541 Baars et al., 2016), considered in the CALIOP retrieval algorithm have been applied in other source
542 areas of mineral particles (see Section 2.3; Figure S1). An additional factor that must be taken into
543 account, is the number of MERRA-2 – CALIOP pairs which is used for the metrics derivation. The
544 corresponding global geographical distribution (Figure S2-i), representative over the period 2007-
545 2015, shows that in areas where the model-satellite agreement is good (Figure 3) the number of
546 common samples is high (>100) in contrast to regions (<50) where the computed metrics are
547 degraded.

548 In order to complete the evaluation of the MERRA-2 dust portion versus CALIOP, the
549 dependency of the level agreement on the spatial representativeness within the $1^\circ \times 1^\circ$ CALIOP grid-
550 cell has also been investigated. Figure S2-ii displays the long-term averaged geographical distribution



551 of the number of CALIOP L2 profiles (up to 23) aggregated for the derivation of the $1^\circ \times 1^\circ$ grid-cell.
552 According to the global map, the maximum number of CALIOP profiles are recorded in the latitudinal
553 band extending from 45° S to 45° N while the “impact” of extended clouds around the equator is
554 apparent. Outside of this zone, the number of profiles used is mainly less than 14 and decreases
555 towards the poles due to the enhanced cloud coverage. The same evaluation metrics presented in
556 Figure 3 have been also computed at planetary scale for individual classes of CALIOP L2 number of
557 profiles (Figure S3). Overall, about 3.4 million pairs (x tick named “ALL” in Figure S3-a) have been
558 found over the period 2007-2015 and are almost equally distributed for bins spanning from 8 to 20
559 while the number of collocated data is higher in the lowermost (≤ 7) and uppermost (≥ 21) tails of the
560 distribution. Based on FB (Figure S3-c), FGE (Figure S3-d) and correlation (Figure S3-e) results it is
561 revealed that the consistency between MERRA-2 and CALIOP gradually improves for higher
562 CALIOP grid-cell representativeness. In quantitative terms, FB decreases from ~ 1.2 to ~ 0.2 , FGE
563 decreases from ~ 1.6 to ~ 0.9 and R increases from ~ 0.5 to ~ 0.8 while the corresponding overall results
564 (i.e., first red bar) are equal to ~ 0.7 , ~ 1.3 and ~ 0.7 , respectively. At global scale, MERRA-2
565 overestimates dust portion by up to 1.5% with respect to CALIOP (Figure S3-b). Among the bin
566 classes, the maximum overestimation ($\sim 2.8\%$) is recorded when four CALIOP profiles are averaged
567 for the derivation of the $1^\circ \times 1^\circ$ cell, while the positive MERRA-2-CALIOP differences become lower
568 than 0.1 when at least 12 CALIOP profiles are considered. Regarding the bias sign, the only exception
569 is observed for cases where 22 or 23 CALIOP profiles are used resulting in slight MERRA-2
570 underestimations.

571 Based on the findings of the Sections 4.1 and 4.2, the MERRA-2 related outputs (AOD, MDF)
572 used in this method, after their quantitative evaluation with MODIS and CALIPSO products, showed
573 reasonable results comparing them on a global scale. In order to provide a deeper assessment of the
574 derived DOD product we have used AERONET AOD and DOD data for an additional evaluation
575 purpose.

576

577 *4.3. Evaluation of MIDAS DOD versus AERONET observations*

578

579 In the present section, we provide an assessment of MODIS L2 AOD and the derived MIDAS
580 DOD against the corresponding AERONET almucantar retrievals as discussed in Section 2.4. The
581 validation of the MODIS quality filtered AOD (Section 2.1) aims at assessing the performance of the
582 input data while for the derived DOD to check the validity of our approach (Section 3.1). An
583 illustration of the MODIS-AERONET collocation is shown in Figure S4. At first, a short discussion
584 is made on the MODIS-AERONET AOD evaluation results, shown in Figure S5, obtained by 59445
585 pairs (Figure S5-ii) collected at 645 ground stations (Figure S5-i) during the period 2007-2016. Based



586 on the 2D histogram scatterplot of Figure S5, the very high correlation ($R=0.894$), the slope ($\alpha=0.929$)
587 which is close to unity and the near-zero offset ($b=0.008$) reveal a remarkable MODIS-AERONET
588 agreement. Overall, MODIS slightly underestimates AOD (-0.003 or -1.741% in absolute and relative
589 percentage terms, respectively) with respect to AERONET. Our results are consistent with those
590 obtained by dedicated global evaluation studies (Levy et al., 2013; Sayer et al., 2013; Sayer et al.,
591 2014) of C006 MODIS AOD product despite the differences regarding the time periods,
592 spatiotemporal collocation criteria, filtering of satellite retrievals based on QA flags and the
593 consideration of AERONET data.

594 The corresponding analysis for DOD is presented at global and station levels in Figures 4 and 5,
595 respectively. As expected, the coincident spaceborne and ground-based DODs collected at 376
596 AERONET stations (red circles in Figure 4-i) are drastically reduced down to 7299 pairs due to the
597 implementation of filters for the determination of DOD on AERONET data (Section 2.4). However,
598 the global scatterplot metrics (Figure 4-ii) are similar to those computed for AOD revealing a very
599 good performance of the MODIS derived DOD. Both datasets are well correlated ($R=0.882$) with
600 MIDAS slight underestimating DOD compared to AERONET (-0.009 or -5.307%). According to our
601 methodology, only the AERONET AODs associated with α lower/equal than/to 0.75 are kept for the
602 evaluation procedure. The defined upper threshold on α values is higher compared to previous
603 findings or applied cut-off levels (e.g. Dey et al., 2004; Tafuro et al., 2006; Reid et al., 2008; Kim et
604 al., 2011; Gkikas et al., 2016). We repeated the analysis by reducing α from 0.75 to 0.25 (results not
605 shown here) and obtained very similar global scatterplot metrics.

606 The evaluation analysis was also performed individually for each station. Figure 5 depicts only
607 sites with at least 30 common MODIS/AERONET observations, thus making the comparison at
608 station level meaningful. This criterion is satisfied in 61 stations, which overall comprise 70% (or
609 5085) of the total population of MODIS-AERONET coincident DODs, and are mostly located over
610 dust sources as well as on areas affected by dust transport, from short to long range. Figure 5-i shows
611 the station-by-station variability of the number of common MODIS/AERONET observations ranging
612 from 100 to 355 (Banizoumbou, Niger) across N. Africa and Middle East whereas in the remaining
613 sites is mainly lower than 70. Between the two datasets, very high R values (up to 0.977) are found
614 in N. Africa, Middle East, outflow regions (Cape Verde, Canary Islands, Mediterranean) and at distant
615 areas (Caribbean Sea) affected by long-range transport. Over the stations located across the Sahel,
616 the maximum RMSE levels (up to 0.243) are recorded (Figure 5-iii) due to the strong load and
617 variability of the Saharan dust plumes. The maximum positive biases (0.133) indicate that the derived
618 MIDAS DOD is overestimated. Several reasons may explain the predominance of positive MIDAS-
619 AERONET differences over the above-mentioned stations taken into account that the MERRA-2 dust
620 portion is adequately reproduced with respect to CALIOP. The first one is related to the MODIS



621 retrieval algorithm itself and more specifically with the applied aerosol models, surface reflectance
622 and cloud screening procedures (Sayer et al., 2013). However, for AOD (results not shown here),
623 small negative biases are observed in agreement with the findings by Sayer et al. (2013) who utilized
624 DB products only. The second factor is the absence of fine DOD on AERONET data which would
625 have reduced the obtained positive differences but its contribution to the total dust AOD it is difficult
626 and probably impossible to be quantified. Similar tendencies, but at a lesser degree, are found for the
627 RMSE and bias scores in the Middle East where the satellite and ground-based DODs are in general
628 well-correlated. In the Mediterranean, the temporal covariation between the two datasets is quite
629 consistent ($R > 0.8$) with the MIDAS DOD being slightly underestimated probably due to the
630 underestimation of the MERRA-2 dust portion.

631 In Asia, few stations are available with sufficient number of MODIS-AERONET collocations in
632 which negative biases are generally recorded both for DOD (Figure 5-iv) and AOD (results not shown
633 here). This agreement indicates that the MODIS AOD underestimation is “transferred” also to DOD
634 and locally can be further enhanced by the MERRA-2 dust portion underestimation (Figure 3-i).
635 Along the western coasts of the United States, the evaluation scores at 5 AERONET sites show that
636 the performance of the retrieved AOD is superior than those for the derived DOD (R : 0.42-0.78, bias:
637 -0.02-0.05, RMSE: 0.03-0.07) attributed to the deficiency of MERRA-2 to reproduce adequately the
638 contribution of dust particles to the total dust aerosol load. Finally, our assessment analysis in the
639 Southern Hemisphere, for stations located in Argentina, Namibia and Australia, indicate slight
640 MODIS-AERONET deviations, spanning from -0.03 (Lucinda) to 0.02 (Gobabeb), and correlations
641 ranging from 0.12 (Fowlers_Gap) to 0.8 (Birdsville).

642

643 *4.4. Intercomparison of MIDAS, MERRA-2 and CALIOP DOD products*

644

645 Following the evaluation of MIDAS DOD against AERONET, the three DOD products derived
646 from MIDAS, MERRA-2 and CALIOP are investigated in parallel. For this purpose, the MERRA-2
647 outputs and MODIS retrievals have been regridded to $1^\circ \times 1^\circ$ grid cells in order to match CALIOP’s
648 spatial resolution while the study period extends from 2007 to 2015, driven again from CALIOP’s
649 temporal availability. Then, the three datasets have been collocated by selecting the coincident pixel
650 for which the temporal deviation between model outputs and satellite overpasses is minimized. The
651 intercomparison has been performed only during daytime conditions and the obtained findings are
652 presented through geographical distributions (Section 4.4.1) and intra-annual timeseries of regional,
653 hemispherical and planetary averages (Section 4.4.2). Finally, it must be clarified that our focus in
654 this part of the analysis is the intercomparison of the different DOD products and not to interpret their



655 spatiotemporal features which will be discussed thoroughly in a companion paper analyzing the
656 DODs from the MIDAS fine resolution dataset.

657

658 4.4.1. *Geographical distributions*

659

660 The annual geographical distributions of CALIOP, MERRA-2 and MIDAS DODs are depicted
661 in Figures 6-i, 6-ii and 6-iii, respectively, while the corresponding global seasonal maps are provided
662 in Figure S6. Among the three datasets, both for annual and seasonal geographical distributions, it is
663 apparent a very good agreement in spatial terms in contrast to the magnitude of the simulated
664 (MERRA-2) and retrieved (MIDAS, CALIOP) DODs. The most evident deviations of MERRA-2
665 (Figure 6-ii) and MIDAS (Figure 6-iii), with respect to CALIOP (Figure 6-i), are encountered across
666 N. Africa forming clear patterns with positive and negative biases over the Sahara and the Sahel,
667 respectively. In particular, MERRA-2 DOD overestimations range from 0.04 to 0.20 while the
668 MIDAS-CALIOP deviations are lower; placing our DOD product between active remote sensing
669 retrievals and reanalysis dataset. A common feature is the location where the maximum
670 “overestimations” are observed. These areas are identified in Algeria, Niger and Chad featuring
671 substantially high dust concentrations. Previous studies relied on satellite (Yu et al., 2010; Kittaka et
672 al., 2011; Ma et al., 2013) and ground-based (Schuster et al., 2012; Omar et al., 2013) observations
673 have noted that CALIOP underestimates AOD over the Sahara. Konsta et al. (2018), who utilized
674 higher and more realistic dust lidar ratio (55 sr; adopted also for the region in the current study), with
675 respect to the aforementioned works (40 sr), reported similar tendencies against MODIS. Therefore,
676 other factors might contribute to the lower lidar-derived DODs over the arid regions of N. Africa. For
677 example, it has been observed that CALIOP can misclassify as clouds very intense dust layers which
678 can also attenuate significantly or totally the emitted laser beam (Yu et al., 2010; Konsta et al., 2018).
679 All these aspects, most likely met over dust sources, act towards reducing the extinction coefficient
680 and may explain the “missing” hotspot on CALIPSO in/around the Bodélé Depression in contrast to
681 single-view, multi-angle and geostationary passive satellite sensors (e.g., Banks and Bridley, 2013;
682 Wei et al., 2019). Across the Sahel, CALIOP provides higher DODs (mainly up to 0.2) both against
683 simulated and satellite products. These differences might be attributed to the misrepresentation of
684 dust sources in MERRA-2 along this zone where vegetation cover has a prominent seasonal cycle
685 (Kergoat et al., 2017). An inaccurate representation of vegetation also impacts the surface reflectance
686 which in turn can introduce critical errors in the retrieval algorithm. Sayer et al. (2013) showed that
687 MODIS overestimates AOD with respect to AERONET while the maximum MIDAS-AERONET
688 negative DOD bias (-0.154) is recorded at Ilorin (Figure 5-iv).



689 Over the eastern Tropical Atlantic Ocean, the difference between CALIOP and MIDAS is
690 negligible whereas MERRA-2 underestimates DOD by up to 0.08. In the Middle East, MERRA-2
691 and MIDAS DODs are higher than those retrieved by CALIOP over the Tigris-Euphrates basin while
692 an opposite tendency, particularly for MIDAS, is found in the interior parts of Saudi Arabia. Lower
693 DODs are also observed by CALIOP over the arid/semi-arid regions, including the Aral Sea,
694 eastwards of the Caspian Sea. This area of the planet is one of the most challenging for passive
695 observations from space due to the terrain complexity prohibiting the accurate characterization of the
696 surface reflectance and type. Such conditions impose artifacts to the retrieval algorithm resulting in
697 unrealistically high MODIS AODs (Klingmüller et al., 2016; see interactive comment posted by
698 Andrew Sayer) that may also affect MERRA-2 via assimilation. Along the mountainous western parts
699 of Iran, CALIPSO DOD is substantially higher than those derived with our methodology while
700 against MERRA-2 the obtained positive or negative differences are close to zero. The largest negative
701 MIDAS-CALIOP differences (exceeding 0.2), not only in Asia but all over the world, are recorded
702 in the Taklamakan Desert whereas the corresponding results between MERRA-2 and CALIOP are
703 somewhat lower. This might be attributed to an inappropriate selection (overestimation) of the lidar
704 ratio taking into account that CALIOP mainly underestimates AOD over the region, dust contribution
705 to the total AOD exceeds 70% (Proestakis et al., 2018), throughout the year, and MDF shows robust
706 consistency (Figure 3). Eastwards of the Asian continent, the situation is reversed and the CALIOP
707 DODs are lower by up to 0.2 when compared to MERRA-2 and MIDAS indicating a weaker trans-
708 Pacific transport, predominant during boreal spring (second row in Figure S6), being in agreement
709 with the findings of Yu et al. (2010) and Ma et al. (2013). In the S. Hemisphere, negative MERRA-
710 2-CALIOP and MIDAS-CALIOP differences are computed in Patagonia, which are not however
711 spatially coherent. On the contrary, in the desert areas of the inland parts of Australia, there is a clear
712 signal of positive MERRA-2-CALIOP deviations, not seen between MIDAS and CALIOP, most
713 likely attributed to the overestimation of aerosol (dust) optical depth by MERRA-2 as it has been
714 recently presented by Mulkavilli et al. (2019). On a global and long-term perspective, based on more
715 than 470000 collocated data, MERRA-2 correlates better with CALIOP than MIDAS ($R=0.740$ vs.
716 0.665), but is more biased (relative bias= 4.264% vs. 9.405%).

717

718 *4.4.2. Planetary, hemispherical and regional intra-annual variability*

719 At a next step of the intercomparison, the variability of the planetary (Figure 7-i) and
720 hemispherical (Figures 7-ii, 7-iii) monthly averages of CALIOP (black curve), MERRA-2 (red curve)
721 and MIDAS (blue curve) DODs were compared. It is clarified that the calculations presented here
722 have been performed, at each considered timescale, following the upper branch shown in Figure 5 of
723 Levy et al. (2009), comprising first a temporal averaging and then a spatial averaging taking into the



724 weight of the grid cell surface area to the total domain area with available data. In the N. Hemisphere,
725 the most evident deviations among the three products occur from March to June when the dust activity
726 is more pronounced (Figure 7-ii). During the high-dust seasons, the DOD peaks are recorded in June,
727 being identical (0.117) for MERRA-2 and MIDAS with CALIOP giving lower levels (0.114). Both
728 the MIDAS/MERRA-2 “temporal consistency” and the CALIOP “underestimation” are mostly valid
729 during boreal spring and summer with few exceptions, highlighted when focus is given on the
730 temporal covariation. Within the course of the year, CALIOP and MERRA-2 DODs gradually
731 increase from January to June while decrease during the second half of the annual cycle. While the
732 trends in MIDAS DOD are similar overall, there is a local minimum observed in May (0.083)
733 resulting in deviations of -0.009 and -0.021 compared to CALIOP and MERRA-2, respectively. On
734 an annual basis (Table 1), the averaged MERRA-2 and MIDAS DODs, for the northern hemisphere,
735 are the same (0.055) and higher by up to 10% than the corresponding CALIOP mean (0.050). In the
736 S. Hemisphere (Figure 7-iii), DODs range at very low levels (up to 0.011), attributed to the low
737 amounts of mineral particles emitted from spatially restricted desert areas, and the limited dust
738 transport over oceanic regions. Despite these low values, there is an annual cycle pattern, which,
739 however, is not commonly reproduced by the three datasets in contrast to the annual means which are
740 almost identical among them (0.007-0.008; Table 1). In particular, MIDAS and MERRA-2 DODs are
741 maximized in February (0.009) while the highest levels for CALIOP are recorded in September
742 (0.011). For all DOD products, the minimum values (slightly less than 0.006) are found in May, which
743 are slightly lower than those observed during April-July (austral winter). At global scale (Figure 7-i),
744 the seasonal patterns of DODs are mainly driven by those of the N. Hemisphere, where the main dust
745 sources of the planet are situated, but the intra-annual cycles of MIDAS and MERRA-2 are not
746 identical with those of GLB in contrast to CALIOP. More specifically, there are two peaks (~0.05,
747 March and June) for MIDAS, flat maximum levels (~0.05) between March and June for MERRA-2
748 while there is a primary (0.048) and a secondary (0.041) maximum in June and March, respectively,
749 for CALIOP DODs. Even though there are month-by-month differences, the CALIOP (0.029),
750 MERRA-2 (0.031) and MIDAS (0.031) annual DODs are very close indicating a sufficient level of
751 agreement among the three datasets (Table 1). Likewise, our findings are almost identical with the
752 global DOD average (0.030) reported by Ridley et al. (2016).

753 The consistency among the three datasets, in terms of DOD magnitude and temporal covariation,
754 is highly dependent on the region of interest. Table 1 lists the computed annual averages as well as
755 their minimum/maximum limits, Figure S7 shows the defined sub-domains and Figure S8 their intra-
756 annual timeseries. The best agreement among MIDAS, CALIOP and MERRA-2 DODs is found along
757 the Tropical Atlantic Ocean, which is affected by Saharan dust transport throughout the year,
758 particularly its eastern sector. In the nearby outflow regions, considerably high DODs (> 0.1) are



759 found between January-August, being maximum in June, as indicated by the three datasets, with slight
760 underestimations in MERRA-2 (Fig. S8-k). Over the western Tropical Atlantic Ocean, the sharp
761 increase of DOD from May to June indicates the arrival of considerable amounts of Saharan particles,
762 which are sustained at high levels in summer and diminish during autumn and winter (Fig. S8-q).
763 This seasonal fluctuation is almost identically reproduced by the spaceborne (MIDAS, CALIOP) and
764 reanalysis (MERRA-2) products. Nevertheless, when the dust activity is well established in the area
765 (boreal summer), there is clear difference on DOD values with higher CALIOP levels compared to
766 MERRA-2 and MIDAS, which are quite similar.

767 Across N. Africa, and particularly in the Bodélé (Fig. S8-a) and W. Sahara (Fig. S8-h), the
768 CALIOP DODs are substantially lower when compared to MIDAS and MERRA-2. In the Bodélé,
769 this is evident for the entire year and in W. Sahara it can be clearly seen during the high-dust boreal
770 summer season. Similar findings are drawn either for other source areas, such as Central Asia (Fig.
771 S8-c), the northern Middle East (Fig. S8-d), the southwest United States (Fig. S8-e) or outflow
772 regions, such as the Mediterranean (Fig. S8-m). Over the Taklamakan (Fig. S8-f) and Gobi (Fig. S8-
773 b) Deserts, the CALIOP DODs are higher than the corresponding MIDAS and MERRA-2 regional
774 averages in April-May. Among the three DOD products, a very good temporal agreement it is found
775 in the Thar Desert (Fig. S8-g), but there are deviations regarding the peak of July which is higher in
776 MIDAS (1.172) than in CALIOP (0.978) and MERRA-2 (0.484), respectively. Over downwind
777 continental areas downwind of E. Asia (Fig. S8-i), only few exceptions break down the consistency
778 between MIDAS and CALIOP and MERRA-2 is able to reproduce the annual cycle but
779 underestimates the intensity of dust loads. In southern Middle East (Fig. S8-n), the reanalysis and the
780 spaceborne lidar DODs are very well correlated and reveal minor differences within the course of the
781 year. MIDAS captures satisfactorily the monthly variability of DOD, despite the local minimum in
782 May, but fails to reproduce the magnitude of the recorded maximum in June. Over the Northern
783 Pacific, Asian dust is transported eastwards during spring affecting nearby (Fig. S8-p) and distant
784 (Fig. S8-j) oceanic areas. The “signal” of this mechanism is clearly evident on MIDAS and MERRA-
785 2 timeseries in contrast to CALIOP which exhibits substantially lower DOD maxima. Moreover, they
786 appear earlier (March) with respect to the other two datasets (April) in the western North Pacific
787 Ocean. Based on MERRA-2 and MIDAS, in the sub-Sahel (Fig. S8-o), a primary and a secondary
788 maximum are recorded in March and October, in agreement with ground-based visibility records
789 (N’Tchayi Mbourou et al., 1997). CALIOP reproduces both peaks, but with a weaker intensity in
790 March compared to MIDAS and MERRA-2. However, throughout the year, the maximum CALIOP
791 DOD is observed in June (a local maximum is also recorded in MIDAS), which might be unrealistic
792 since it is not expected the accumulation of dust particles during summer months, when the
793 precipitation heights in the area are maximized. Saharan dust aerosols, under the impact of the



794 northeasterly harmattan winds, are carried over the Gulf of Guinea (Fig. S8-l) during boreal winter,
795 although DODs among the three datasets reveal a noticeable variability in terms of intensity.

796

797 4.5. MIDAS DOD global climatology

798

799 The annual and seasonal DOD patterns averaged over the period 2007 – 2016 are illustrated in
800 Figures 8 and 9. Among the desert areas of the planet, the most intense dust loads (DODs up to ~1.2;
801 Fig. 8) are hosted across the Sahara Desert and particularly in the Bodélé Depression of the northern
802 Lake Chad Basin (Washington et al., 2003). Over the region, these high DODs are sustained
803 throughout the year (Fig. 9) while due the prevailing meteorological conditions, during MAM (Fig.
804 9-ii) and JJA (Fig. 9-iii), mineral particles are transported westwards, along the Sahel, contributing
805 to the locally emitted anthropogenic dust (Ginoux et al., 2012). Substantial high climatological DODs
806 (up to 0.6; Fig. 8) are recorded in the western sector of Sahara, in contrast to the eastern parts,
807 attributed to the accumulation of dust aerosols primarily in JJA (Fig. 9-iii) and secondarily in MAM
808 (Fig. 9-ii), under the impact of the Saharan Heat Low (Schepanski et al., 2017). Saharan dust is
809 subjected to short-range transport affecting frequently the nearby maritime areas of the Gulf of
810 Guinea (Ben-Ami et al., 2009), the Mediterranean Sea (Gkikas et al., 2015) as well the Red Sea
811 (Banks et al., 2017). Nevertheless, the strongest signal of Saharan dust transport appears over the
812 Tropical Atlantic Ocean with massive loads of mineral particles, confined within the Saharan Air
813 Layer (SAL; Kanitz et al., 2014), reaching the Caribbean Sea (Prospero, 1999), under the impact of
814 the trade winds. The characteristics of the transatlantic dust transport reveal a remarkable intra-annual
815 variation (Fig. 9) as it concerns plumes' latitudinal position, longitudinal extension and intensity,
816 being maximum during boreal summer (Fig. 9-iii).

817 Dust activity over the Middle East is more pronounced in a “zone” extending from the alluvial
818 plain of the Tigris-Euphrates River to the southern parts of the Arabian Peninsula (Fig. 8), through
819 the eastern flat-lands of Saudi Arabia (Hamidi et al., 2013). Mineral particles emitted from these
820 sources affect also the Persian Gulf (Gianakopoulou and Toumi, 2011) and the Red Sea (Banks et al.,
821 2017); however, the major transport pattern is recorded across the northern Arabian Sea in JJA (Fig.
822 9-iii), when dust plumes can reach the western coasts of India (Ramaswamy et al., 2017). In the Asian
823 continent, the Taklamakan Desert (Ge et al., 2014), situated in the Tarim basin (NW China), consists
824 one of the strongest dust source of the planet yielding DODs up to 1 during spring (Fig. 9-ii). These
825 intensities are substantially higher than those recorded in the Gobi Desert, situated eastwards in the
826 same latitudinal band, due to the different composition of the erodible soils (Sun et al., 2013).
827 Midlatitude cyclones, propagating eastwards during springtime (Fig. 9-ii), mobilize dust emission
828 from both sources inducing uplifting and subsequently advection of mineral particles towards the



829 continental E. Asia (Yu et al., 2019) as well as over the north Pacific Ocean (Yu et al., 2008) and
830 exceptionally over the United States (Husar et al., 2001). Other hotspots of dust activity in Asia, are
831 recorded in the central parts (Li and Sokolik, 2018) and in the Sistan Basin (Alizadeh Choobari et al.,
832 2013). Dust aerosols originating from agricultural activities along the Indus River basin (Ginoux et
833 al., 2012) and natural processes in the Thar Desert (Proestakis et al., 2018) result in the accumulation
834 of mineral particles in the Pakistan-India borders while under favorable meteorological conditions
835 these loads are carried towards the Indo-Gangetic plain mainly during the pre-monsoon season (Dey
836 et al., 2004). In North America, dust production becomes more evident in the southwestern United
837 States and northwest Mexico in regional terms and during spring within the course of the year (Fig.
838 9-ii). However, DODs are mostly lower than 0.2, with few local exceedances, indicating weak dust
839 emission from the natural (Mojave and Sonoran Deserts; Hand et al., 2017) and anthropogenic
840 (Chihuahuan Desert and Southern Great Plains; Hand et al., 2016) dust sources of the region. Between
841 the two hemispheres, there is a clear contrast in DODs, being substantially lower in the S.
842 Hemisphere, attributed to the weaker processes triggering dust emission from the spatially restricted
843 deserts located in S. Africa (Bryant et al., 2007), S. America (Gassó and Torres, 2019) and in the
844 interior parts of Australia (Prospero et al., 2002).

845 Apart from the global climatological DOD pattern in Figure 8-i, the corresponding distributions
846 of the total uncertainty (taking into account the propagation of each individual DOD uncertainty to
847 the average grid cell value as well as the sampling uncertainty expressed by the standard error) and
848 the temporal availability are shown in Figs. 8-ii and -iii, respectively, thus allowing to assess the
849 accuracy of the derived product as well as its representativeness throughout the study period (2007-
850 2016). More than 70% of satellite retrievals, with respect to the full period, are participating in the
851 calculation of the mean DODs (Fig. 8-i) over the cloud-free desert areas while over dust-affected
852 downwind regions the corresponding percentages range from 30 to 60% (Fig. 8-iii). Regarding the
853 total DOD uncertainty (Fig. 8-ii), the spatial pattern indicates maximum absolute levels (up to 0.1) in
854 the sub-Sahel and in the Gulf of Guinea whereas similar values are found in the Taklamakan Desert
855 and lower in the Tropical Atlantic. On a seasonal basis (Figure S9), the spatial features of DOD
856 uncertainties are driven by those of DOD (Figure 9) over sources and receptor areas while MIDAS
857 DODs are similarly less reliable, in absolute terms, over regions affected rarely by dust loads.
858 However, in relative terms, across deserts and areas subjected to dust transport, the DOD uncertainty
859 with respect to the obtained long-term averages, throughout the year, is mainly lower than 20% and
860 over regions with weak dust loads is higher than 60%. This contrast is attributed to the larger number
861 of available DODs over/nearby the deserts, where dust signal is maximized, as well as to the lower
862 $\Delta(\text{DOD})$ resulting from the lower relative AOD errors and the better MDF performance there.

863



864 5. Summary and conclusions

865

866 In the current study, we presented the MIDAS (ModIs Dust AeroSol) dust optical depth (DOD)
867 dataset, combining MODIS-Aqua AOD and DOD-to-AOD ratio extracted from collocated MERRA-
868 2 reanalysis outputs. The derived fine resolution ($0.1^\circ \times 0.1^\circ$) global dataset, valid for a decade (2007-
869 2016), provides DOD both over continental and oceanic areas, in contrast to similar available satellite
870 products restricted over land surfaces (Ginoux et al., 2012), thus making feasible a thorough
871 description of dust loads not only over the sources but also over downwind regions where transport,
872 from short- to long-range, is taking place. Reanalysis datasets, spanning through decades and
873 available at high temporal frequency, can fulfill such tasks; however, their coarser spatial resolution
874 imposes a restriction when investigating mineral loads' features at finer spatial scales. Our developed
875 DOD product aims at complementing existing observational gaps and can be exploited in a variety of
876 studies related to dust climatology and trends, evaluation of atmospheric-dust models, estimation of
877 dust radiative effects and assessment of the associated impacts as well as on improving dust
878 forecasting and monitoring via data assimilation.

879 The core concept of the applied methodology relies on the utilization of MODIS AOD and
880 MERRA-2 DOD-to-AOD ratio for the derivation of DOD on MODIS swaths. Nevertheless, two prior
881 steps have been done ensuring the necessity and the validity of the proposed method. First, the
882 MODIS AODs have been compared against the corresponding MERRA-2 outputs in order to justify
883 that these two datasets are not similar, thus avoiding the consideration of a dataset of low temporal
884 frequency (one overpass per day) rather than hourly reanalysis outputs. According to our results, the
885 spatial AOD global patterns are commonly reproduced by MODIS and MERRA-2; however, there
886 are evident differences in the aerosols loads. For example, MERRA-2 shows a higher AOD across N.
887 Africa by up to 0.25, and over other dusty regions. Over biomass burning areas (e.g. Amazon, Central
888 Africa) and industrialized regions (E. Asia) the AOD can be smaller in MERRA-2 by up to 0.3. Over
889 oceans, the majority of MERRA-2 – MODIS differences are very small, except in the case of the
890 Tropical Atlantic Ocean where the MODIS AODs are higher than the corresponding simulated levels
891 by up to 0.05.

892 The second prior step comprises the evaluation of the MERRA-2 MDF against reference values
893 obtained by the columnar integration of quality assured dust and non-dust CALIOP profiles. Over
894 dust-abundant areas extending across the “dust belt”, MERRA-2 reproduces adequately the
895 magnitude of dust portion as indicated by the calculated primary statistics (bias, FB, FGE) with the
896 maximum underestimations (up to 10%) being observed in Asian deserts. The agreement between
897 MERRA-2 and CALIOP is reduced in the main dust regions of N. America and in the S. Hemisphere.
898 Regarding the temporal covariation of the observed and simulated dust portions, over the period 2007-



899 2015, moderate R values (up to 0.5) are computed above the sources, attributed to the high
900 spatiotemporal variability of the emission processes. On the contrary, the correlation increases
901 substantially (up to 0.9) over downwind maritime regions (Tropical Atlantic Ocean, north Pacific
902 Ocean, Arabian Sea, Mediterranean Sea) where the main dust transport paths are recorded. Apart
903 from the geographical dependency of the level of agreement between MERRA-2 and CALIOP DOD-
904 to-AOD ratios, we also investigated the impact of the spatial representativeness of the CALIOP
905 observations. Through this analysis, we revealed that for an increasing number of CALIOP L2
906 profiles (from 1 to 23), aggregated for the derivation of the $1^\circ \times 1^\circ$ grid cell, the computed metrics
907 converge towards their ideal scores.

908 Finally, the obtained MIDAS DOD was evaluated against AERONET retrievals and compared
909 with CALIOP and MERRA-2 DODs. AEROENT observations were processed to minimize the
910 contribution of other aerosol species and assuming that dust loads are mainly consist of coarse
911 particles (their radii is larger than the defined inflection point). Overall, the agreement between ~7300
912 MIDAS-AERONET pairs resides is very high ($R=0.882$), whereas the satellite DODs are lower by
913 ~5% with respect to the ground-based ones. At station level, the R values are mainly above 0.8 at
914 most sites of the N. Hemisphere (except western US) while they don't exceed 0.5 in the S.
915 Hemisphere. Moreover, positive MIDAS-AERONET deviations (up to 0.133) are mainly
916 encountered in N. Africa and Middle East in contrast to negative values (down to -0.154) recorded at
917 the remaining sites. Based on the annual and seasonal global DOD patterns averaged over the period
918 2007-2015 the locations with the maximum DODs are in a good agreement among the three datasets.
919 Nevertheless, in many regions (e.g., Bodélé, sub-Sahel, north Pacific Ocean) there are deviations on
920 the intensity of dust loads, attributed to the inherent weaknesses of DOD derivation techniques based
921 on different approaches. Despite the regional dependency of biases among the three datasets, the
922 collocated global long-term averaged DODs are very similar (0.029 for CALIOP, 0.031 for MERRA-
923 2 and MIDAS) and very close to those reported (0.030) by Ridley et al. (2016). In the S. Hemisphere
924 the corresponding levels (0.007-0.008) slightly differ for the three datasets, whereas in the N.
925 Hemisphere, CALIOP DODs (0.050) are lower by 10% with respect to MIDAS and MERRA-2
926 hemispherical averages (0.055).

927 As a demonstration of the MIDAS dataset, a brief discussion about dust loads' regime at global
928 scale is made by analyzing the annual and seasonal DOD patterns. The most pronounced dust activity
929 recorded in the Bodélé Depression of the northern Lake Chad Basin (DODs up to ~1.2), across the
930 Sahel (DODs up to 0.8), in western parts of the Sahara Desert (DODs up to 0.6), in the eastern parts
931 of the Arabian Peninsula (DODs up to ~1), along the Indus river basin (DODs up to 0.8) and in the
932 Taklamakan Desert (DODs up to ~1). On the contrary, the weaker emission mechanisms triggering
933 dust mobilization over the spatially limited sources of Patagonia, South Africa and interior arid areas



934 of Australia do not favor the accumulation of mineral particles at large amounts (DODs up to 0.4 at
935 local hotspots), even during high-dust seasons. Over oceans, the main pathways of long-range dust
936 transport are observed along the tropical Atlantic and the northern Pacific, revealing a remarkable
937 variation, within the course of the year, in terms of intensity, latitudinal position and range. Finally,
938 the Mediterranean and the Arabian Sea are affected by advected dust plumes originating from N.
939 Africa and Middle East, respectively. Based on the performed uncertainty analysis, the MIDAS DOD
940 product, within the course of the year, is highly reliable (less than 0.1 and 20% in absolute and relative
941 terms, respectively) over dust rich regions and becomes more uncertain (>60%) in areas where the
942 existence of dust loads is not frequent. This contradiction is interpreted by the stronger “signal” of
943 dust loads and the larger data availability thus converging towards lower measurement and sampling
944 uncertainties.

945 The exploitation of the MIDAS DOD product will be expanded in scheduled and under
946 preparation studies. At present, focus is given on: (i) the DOD climatology over dust sources and
947 downwind regions, (ii) the implementation of the MIDAS dataset in the DA scheme of the NMMB-
948 MONARCH model (Di Tomaso et al., 2017) and (iii) the estimation of dust radiative effects and the
949 associated impacts on solar energy production, in North Africa and Middle East, upgrading the work
950 of Kosmopoulos et al. (2018).

951

952 **Acknowledgments**

953 The DUST-GLASS project has received funding from the European Union’s Horizon 2020 Research
954 and Innovation programme under the Marie Skłodowska-Curie grant agreement No. 749461. The
955 authors acknowledge support from the EU COST Action CA16202 “International Network to
956 Encourage the Use of Monitoring and Forecasting Dust Products (inDust). We would like to thank
957 the principal investigators maintaining the AERONET sites used in the present work. We thank the
958 NASA CALIPSO team and NASA/LaRC/ASDC for making available the CALIPSO products which
959 are used to build the LIVAS products and ESA which funded the LIVAS project (contract no.
960 4000104106/11/NL/FF/fk). We are grateful to the AERIS/ICARE Data and Services Center for
961 providing access to the CALIPSO data used and their computational center ([http://www.icare.univ-
962 lille1.fr/](http://www.icare.univ-lille1.fr/), last access: 8 August 2019). Vassilis Amiridis acknowledges support by the European
963 Research Council (grant no. 725698, D-TECT). Eleni Marinou acknowledges support by the
964 Deutscher Akademischer Austauschdienst (grant no. 57370121). Carlos Pérez García-Pando
965 acknowledges support by the European Research Council (grant no. 773051, FRAGMENT), the AXA
966 Research Fund, and the Spanish Ministry of Science, Innovation and Universities (RYC-2015-18690
967 and CGL2017-88911-R) and the DustClim Project as part of ERA4CS, an ERA-NET initiated by JPI
968 Climate, and funded by FORMAS (SE), DLR (DE), BMWFW (AT), IFD (DK), MINECO (ES), ANR



969 (FR) with co-funding by the European Union (Grant 690462). We acknowledge support of this work
970 by the project “PANhellenic infrastructure for Atmospheric Composition and climatE change” (MIS
971 5021516) which is implemented under the Action “Reinforcement of the Research and Innovation
972 Infrastructure”, funded by the Operational Programme “Competitiveness, Entrepreneurship and
973 Innovation” (NSRF 2014-2020) and co-financed by Greece and the European Union (European
974 Regional Development Fund). The authors would like to thank Dr. Andrew Mark Sayer for his
975 valuable and constructive comments. The authors would like also to thank Thanasis Georgiou for
976 developing the ftp server where the MIDAS dataset is stored.

977

978 **Data availability**

979

980 The MIDAS dataset is available at <https://doi.org/10.5281/zenodo.3719222>

981

982 **References**

983

984 Alizadeh Choobari, O., Zawar-Reza, P., and Sturman, A.: Low level jet intensification by mineral
985 dust aerosols, *Ann. Geophys.*, 31, 625–632, <https://doi.org/10.5194/angeo-31-625-2013>, 2013.

986

987 Amiridis, V., Wandinger, U., Marinou, E., Giannakaki, E., Tsekeri, A., Basart, S., Kazadzis, S.,
988 Gkikas, A., Taylor, M., Baldasano, J., and Ansmann, A.: Optimizing CALIPSO Saharan dust
989 retrievals, *Atmos. Chem. Phys.*, 13, 12089–12106, <https://doi.org/10.5194/acp-13-12089-2013>, 2013.

990

991 Amiridis, V., Marinou, E., Tsekeri, A., Wandinger, U., Schwarz, A., Giannakaki, E., Mamouri, R.,
992 Kokkalis, P., Biniotoglou, I., Solomos, S., Herekakis, T., Kazadzis, S., Gerasopoulos, E., Proestakis,
993 E., Kottas, M., Balis, D., Papayannis, A., Kontoes, C., Kourtidis, K., Papagiannopoulos, N., Mona,
994 L., Pappalardo, G., Le Rille, O., and Ansmann, A.: LIVAS: a 3-D multi-wavelength aerosol/cloud
995 database based on CALIPSO and EARLINET, *Atmos. Chem. Phys.*, 15, 7127–7153,
996 <https://doi.org/10.5194/acp-15-7127-2015>, 2015.

997

998 Anderson, T. L., Wu, Y., Chu, D. A., Schmid, B., Redemann, J., and Dubovik, O.: Testing the MODIS
999 satellite retrieval of aerosol fine-mode fraction, *J. Geophys. Res.*, 110, D18204,
1000 [doi:10.1029/2005JD005978](https://doi.org/10.1029/2005JD005978), 2005.

1001

1002 Baars, H., Kanitz, T., Engelmann, R., Althausen, D., Heese, B., Komppula, M., Preissler, J., Tesche,
1003 M., Ansmann, A., Wandinger, U., Lim, J.-H., Ahn, J. Y., Stachlewska, I. S., Amiridis, V., Marinou,



- 1004 E., Seifert, P., Hofer, J., Skupin, A., Schneider, F., Bohlmann, S., Foth, A., Bley, S., Pfuller, A.,
1005 Giannakaki, E., Lihavainen, H., Viisanen, Y., Hooda, R. K., Pereira, S. N., Bortoli, D., Wagner, F.,
1006 Mattis, I., Janicka, L., Markowicz, K. M., Achtert, P., Artaxo, P., Pauliquevis, T., Souza, R. A. F.,
1007 Sharma, V. P., van Zyl, P. G., Beukes, J. P., Sun, J., Rohwer, E. G., Deng, R., Mamouri, R.-E. and
1008 Zamorano, F.: An overview of the first decade of Polly(NET): an emerging network of automated
1009 Raman-polarization lidars for continuous aerosol profiling, *Atmos. Chem. Phys.*, 16(8), 5111–5137,
1010 doi:10.5194/acp-16-5111-2016, 2016.
- 1011
- 1012 Banks, J. R. and Brindley, H. E.: Evaluation of MSG-SEVIRI mineral dust retrieval products over
1013 Africa and the Middle East, *Remote Sensing of Environment*, 128, 58–73,
1014 doi:10.1016/j.rse.2012.07.017, 2013.
- 1015
- 1016 Banks, J. R., Brindley, H. E., Flamant, C., Garay, M. J., Hsu, N. C., Kalashnikova, O. V., Klüser, L.,
1017 and Sayer, A. M.: Intercomparison of satellite dust retrieval products over the west African Sahara
1018 during the Fennec campaign in Jun 2011, *Remote Sens. Environ.*, 136, 99–116, 2013.
- 1019
- 1020 Banks, J. R., Brindley, H. E., Stenchikov, G., and Schepanski, K.: Satellite retrievals of dust aerosol
1021 over the Red Sea and the Persian Gulf (2005–2015), *Atmos. Chem. Phys.*, 17, 3987–4003,
1022 <https://doi.org/10.5194/acp-17-3987-2017>, 2017.
- 1023
- 1024 Basart, S., Pérez, C., Nickovic, S., Cuevas, E., and Baldasano, J. M.: Development and evaluation of
1025 the BSC-DREAM8b dust regional model over Northern Africa, the Mediterranean and the Middle
1026 East, *Tellus B*, 64, 18539, doi:10.3402/tellusb.v64i0.18539, 2012.
- 1027
- 1028 Ben-Ami, Y., Koren, I., and Altaratz, O.: Patterns of North African dust transport over the Atlantic:
1029 winter vs. summer, based on CALIPSO first year data, *Atmos. Chem. Phys.*, 9, 7867–7875,
1030 <https://doi.org/10.5194/acp-9-7867-2009>, 2009.
- 1031
- 1032 Benedetti, A., Morcrette, J.-J., Boucher, O., Dethof, A., Engelen, R. J., Fisher, M., Flentje, H.,
1033 Huneus, N., Jones, L., Kaiser, J. W., Kinne, S., Mangold, A., Razinger, M., Simmons, A. J., Suttie,
1034 M., and the GEMS-AER team: Aerosol analysis and forecast in the European Centre for Medium-
1035 Range Weather Forecasts Integrated Forecast System: 2. Data assimilation, *J. Geophys. Res.*, 114,
1036 D13205, doi:10.1029/2008JD011115, 2009.
- 1037



- 1038 Bond, T. C., Doherty, S. J., Fahey, D. W., Forster, P. M., Berntsen, T., DeAngelo, B. J., Flanner, M.
1039 G., Ghan, S., Kärcher, B., Koch, D., Kinne, S., Kondo, Y., Quinn, P. K., Sarofim, M. C., Schultz, M.
1040 G., Schulz, M., Venkataraman, C., Zhang, H., Zhang, S., Bellouin, N., Guttikunda, S. K., Hopke, P.
1041 K., Jacobson, M. Z., Kaiser, J. W., Klimont, Z., Lohmann, U., Schwarz, J. P., Shindell, D., Storelvmo,
1042 T., Warrent, S. G., and Zender, C. S.: Bounding the role of black carbon in the climate system: A
1043 scientific assessment, *J. Geophys. Res.*, 118, 5380–5552, 2013.
- 1044
- 1045 Bryant, R. G., Bigg, G. R., Mahowald, N. M., Eckardt, F. D., and Ross S. G.: Dust emission response
1046 to climate in southern Africa, *J. Geophys. Res.*, 112, D09207, doi:10.1029/2005JD007025, 2007.
- 1047
- 1048 Buchard, V., da Silva, A. M., Colarco, P. R., Darmenov, A., Randles, C. A., Govindaraju, R., Torres,
1049 O., Campbell, J., and Spurr, R.: Using the OMI aerosol index and absorption aerosol optical depth to
1050 evaluate the NASA MERRA Aerosol Reanalysis, *Atmos. Chem. Phys.*, 15, 5743–5760,
1051 <https://doi.org/10.5194/acp15-5743-2015>, 2015.
- 1052
- 1053 Buchard, V., Randles, C.A., da Silva, A.M., Darmenov, A., Colarco, P.R., Govindaraju, R., Ferrare,
1054 R., Hair, J., Beyersdorf, A.J., Ziemba, L.D. and Yu, H.: The MERRA-2 aerosol reanalysis, 1980
1055 onward. Part II: Evaluation and case studies. *Journal of Climate*, 30, 6851–6872.
1056 <https://doi.org/10.1175/JCLI-D-16-0613>, 2017.
- 1057
- 1058 Bullard, J. E., Baddock, M., Bradwell, T., Crusius, J., Darlington, E., Gaiero, D., Gassó, S.,
1059 Gisladottir, G., Hodgkins, R., McCulloch, R., McKenna-Neuman, C., Mockford, T., Stewart, H., and
1060 Thorsteinsson, T.: High-latitude dust in the Earth system, *Rev. Geophys.*, 54, 447–485,
1061 <https://doi.org/10.1002/2016RG000518>, 2016.
- 1062
- 1063 Burton, S. P., Hair, J. W., Kahnert, M., Ferrare, R. A., Hostetler, C. A., Cook, A. L., Harper, D. B.,
1064 Berkoff, T. A., Seaman, S. T., Collins, J. E., Fenn, M. A. and Rogers, R. R.: Observations of the
1065 spectral dependence of linear particle depolarization ratio of aerosols using NASA Langley airborne
1066 High Spectral Resolution Lidar, *Atmos. Chem. Phys.*, 15(23), 13453–13473, doi:10.5194/acp-15-
1067 13453-2015, 2015.
- 1068
- 1069 Chen, S., Huang, J., Kang, L., Wang, H., Ma, X., He, Y., Yuan, T., Yang, B., Huang, Z., and Zhang,
1070 G.: Emission, transport, and radiative effects of mineral dust from the Taklimakan and Gobi deserts:
1071 comparison of measurements and model results, *Atmos. Chem. Phys.*, 17, 2401–2421,
1072 <https://doi.org/10.5194/acp-17-2401-2017>, 2017.



1073

1074 Chin, M., Ginoux, P., Kinne, S., Torres, O., Holben, B. N., Duncan, D. N., Martin, R. V., Logan, J.
1075 A., Higurashi, H., and Nakajima, T.: Tropospheric aerosol optical thickness from the GOCART
1076 model and comparisons with satellite and Sun photometer measurements, *J. Atmos. Sci.*, 59, 451–
1077 483, [https://doi.org/10.1175/1520-0469\(2002\)059<0461:TAOTFT>2.0.CO;2](https://doi.org/10.1175/1520-0469(2002)059<0461:TAOTFT>2.0.CO;2), 2002.

1078

1079 Chin, M., Diehl, T., Tan, Q., Prospero, J. M., Kahn, R. A., Remer, L. A., Yu, H., Sayer, A. M., Bian,
1080 H., Geogdzhayev, I. V., Holben, B. N., Howell, S. G., Huebert, B. J., Hsu, N. C., Kim, D., Kucsera,
1081 T. L., Levy, R. C., Mishchenko, M. I., Pan, X., Quinn, P. K., Schuster, G. L., Streets, D. G., Strode,
1082 S. A., Torres, O., and Zhao, X.-P.: Multi-decadal aerosol variations from 1980 to 2009: a perspective
1083 from observations and a global model, *Atmos. Chem. Phys.*, 14, 3657–3690,
1084 <https://doi.org/10.5194/acp-14-3657-2014>, 2014.

1085

1086 Colarco, P., da Silva, A., Chin, M., and Diehl, T.: Online simulations of global aerosol distributions
1087 in the NASA GEOS-4 model and comparisons to satellite and ground-based aerosol optical depth, *J.*
1088 *Geophys. Res.*, 115, D14207, <https://doi.org/10.1029/2009JD012820>, 2010.

1089

1090 Colarco, P. R., Nowottnick, E. P., Randles, C. A., Yi, B., Yang, P., Kim, K.-M., Smith, J. A., and
1091 Bardeen, C. G.: Impact of radiatively interactive dust aerosols in the NASA GEOS-5 climate model:
1092 Sensitivity to dust particle shape and refractive index, *J. Geophys. Res.-Atmos.*, 119, 753–786,
1093 <https://doi.org/10.1002/2013JD020046>, 2014.

1094

1095 de Leeuw, G., Sogacheva, L., Rodriguez, E., Kourtidis, K., Georgoulas, A. K., Alexandri, G.,
1096 Amiridis, V., Proestakis, E., Marinou, E., Xue, Y., and van der A, R.: Two decades of satellite
1097 observations of AOD over mainland China using ATSR-2, AATSR and MODIS/Terra: data set
1098 evaluation and large-scale patterns, *Atmos. Chem. Phys.*, 18, 1573–1592, [https://doi.org/10.5194/acp-](https://doi.org/10.5194/acp-18-1573-2018)
1099 18-1573-2018, 2018.

1100

1101 Dey, S. and Di Girolamo, L.: A climatology of aerosol optical and microphysical properties over the
1102 Indian subcontinent from 9 years (2000–2008) of Multiangle Imaging Spectroradiometer (MISR)
1103 data, *J. Geophys. Res.-Atmos.*, 115, D15204, <https://doi.org/10.1029/2009JD013395>, 2010.

1104

1105 Dey, S., Tripathi, S. N., Singh, R. P., and Holben, B. N.: Influence of dust storms on the aerosol
1106 optical properties over the Indo-Gangetic basin, *J. Geophys. Res.-Atmos.*, 109, 1–10,
1107 doi:10.1029/2004jd004924, 2004.



1108

1109 Di Tomaso, E., Schutgens, N. A. J., Jorba, O., and Pérez García-Pando, C.: Assimilation of MODIS
1110 Dark Target and Deep Blue observations in the dust aerosol component of NMMB-MONARCH
1111 version 1.0, *Geosci. Model Dev.*, 10, 1107-1129, <https://doi.org/10.5194/gmd-10-1107-2017>, 2017.

1112

1113 Diehl, T., Heil, A., Chin, M., Pan, X., Streets, D., Schultz, M., and Kinne, S.: Anthropogenic, biomass
1114 burning, and volcanic emissions of black carbon, organic carbon, and SO₂ from 1980 to 2010 for
1115 hindcast model experiments, *Atmos. Chem. Phys. Discuss.*, 12, 24895–24954,
1116 <https://doi.org/10.5194/acpd-12-24895-2012>, 2012.

1117

1118 Du, Y., Xu, X., Chu, M., Guo, Y., and Wang, J.: Air particulate matter and cardiovascular disease:
1119 the epidemiological, biomedical and clinical evidence, *J. Thorac. Dis.*, 8, E8,
1120 <https://doi.org/10.3978/j.issn.2072-1439.2015.11.37>, 2016.

1121

1122 Dubovik, O. and King, M. D.: A flexible inversion algorithm for retrieval of aerosol optical properties
1123 from Sun and sky radiance measurements, *J. Geophys. Res.*, 105, 20673–
1124 20696, <https://doi.org/10.1029/2000JD900282>, 2000.

1125

1126 Dubovik, O., Sinyuk, A., Lapyonok, T., Holben, B. N., Mishchenko, M., Yang, P., Eck, T. F., Volten,
1127 H., Munoz, O., Veihelmann, B., and Van der Zande, W. J.: Application of spheroid models to account
1128 for aerosol particle nonsphericity in remote sensing of desert dust, *J. Geophys. Res.-Atmos.*, 111,
1129 D11208, <https://doi.org/10.1029/2005JD006619>, 2006.

1130

1131 Eck, T. F., Holben, B. N., Sinyuk, A., Pinker, R. T., Goloub, P., Chen, H., Chatenet, B., Li, Z., Singh,
1132 R. P., and Tripathi, S. N.: Climatological aspects of the optical properties of fine/coarse mode aerosol
1133 mixtures, *J. Geophys. Res.-Atmos.*, 115, 19205, <https://doi.org/10.1029/2010JD014002>, 2010.

1134

1135 Ekström, M., McTainsh, G. H. and Chappell, A.: Australian dust storms: temporal trends and
1136 relationships with synoptic pressure distributions (1960–99), *Int. J. Climatol.*, 24, 1581–1599,
1137 doi:10.1002/joc.1072, 2004.

1138

1139 Engelstaedter, S., Tegen, I., and Washington, R.: North African dust emissions and transport, *Earth-
1140 Sci. Rev.*, 79, 73–100, <https://doi.org/10.1016/j.earscirev.2006.06.004>, 2006.

1141



- 1142 Farahat, A.: Comparative analysis of MODIS, MISR, and AERONET climatology over the Middle
1143 East and North Africa, *Ann. Geophys.*, 37, 49–64, <https://doi.org/10.5194/angeo-37-49-2019>, 2019.
1144
- 1145 Fiedler, S., Schepanski, K., Heinold, B., Knippertz, P., and Tegen, I.: Climatology of nocturnal low-
1146 level jets over North Africa and implications for modeling mineral dust emission, *J. Geophys. Res.-*
1147 *Atmos.*, 118, 6100–6121, 2013.
1148
- 1149 Flaounas, E., Kotroni, V., Lagouvardos, K., Kazadzis, S., Gkikas, A., and Hatzianastassiou, N.:
1150 Cyclone contribution to dust transport over the Mediterranean region, *Atmos. Sci. Lett.*, 16, 473–478,
1151 [doi:10.1002/asl.584](https://doi.org/10.1002/asl.584), 2015.
1152
- 1153 Fotiadi, A., Hatzianastassiou, N., Drakakis, E., Matsoukas, C., Pavlakis, K. G., Hatzidimitriou, D.,
1154 Gerasopoulos, E., Mihalopoulos, N., and Vardavas, I.: Aerosol physical and optical properties in the
1155 Eastern Mediterranean Basin, Crete, from Aerosol Robotic Network data, *Atmos. Chem. Phys.*, 6,
1156 5399–5413, <https://doi.org/10.5194/acp-6-5399-2006>, 2006.
1157
- 1158 Freudenthaler, V., Esselborn, M., Wiegner, M., Heese, B., Tesche, M., Ansmann, A., Mueller, D.,
1159 Althausen, D., Wirth, M., Fix, A., Ehret, G., Knippertz, P., Toledano, C., Gasteiger, J., Garhammer,
1160 M. and Seefeldner, A.: Depolarization ratio profiling at several wavelengths in pure Saharan dust
1161 during SAMUM 2006, *Tellus Ser. B-Chem. Phys. Meteorol.*, 61(1), 165–179, [doi:10.1111/j.1600-](https://doi.org/10.1111/j.1600-0889.2008.00396.x)
1162 [0889.2008.00396.x](https://doi.org/10.1111/j.1600-0889.2008.00396.x), 2009.
1163
- 1164 Gassó, S., & Torres, O.: Temporal characterization of dust activity in the Central Patagonia desert
1165 (years 1964–2017), *Journal of Geophysical Research: Atmospheres*, 124, 3417– 3434,
1166 <https://doi.org/10.1029/2018JD030209>.
1167
- 1168 Ge, J. M., Huang, J. P., Xu, C. P., Qi, Y. L., and Liu, H. Y.: Characteristics of Taklimakan dust
1169 emission and distribution: a satellite and reanalysis field perspective, *J. Geophys. Res.-Atmos.*, 119,
1170 11772–11783, <https://doi.org/10.1002/2014JD022280>, 2014.
1171
- 1172 Gelaro, R., McCarty, W., Suárez, M. J., Todling, R., Molod, A., Takacs, L., Randles, C. A., Darmenov,
1173 A., Bosilovich, M. G., Reichle, R., Wargan, K., Coy, L., Cullather, R., Draper, C., Akella, S.,
1174 Buchard, V., Conaty, A., da Silva, A. M., Gu, W., Kim, G., Koster, R., Lucchesi, R., Merkova, D.,
1175 Nielsen, J. E., Partyka, G., Pawson, S., Putman, W., Rienecker, M., Schubert, S. D., Sienkiewicz, M.,



- 1176 and Zhao, B.: The Modern-Era Retrospective Analysis for Research and Applications, Version 2
1177 (MERRA-2), *J. Climate*, 30, 5419–5454, <https://doi.org/10.1175/JCLI-D-16-0758.1>, 2017.
- 1178
- 1179 Georgoulas, A. K., Alexandri, G., Kourtidis, K. A., Lelieveld, J., Zanis, P., Pöschl, U., Levy, R.,
1180 Amiridis, V., Marinou, E., and Tsikerdekis, A.: Spatiotemporal variability and contribution of
1181 different aerosol types to the aerosol optical depth over the Eastern Mediterranean, *Atmos. Chem.*
1182 *Phys.*, 16, 13853–13884, doi:10.5194/acp-16-13853-2016, 2016.
- 1183
- 1184 Georgoulas, A. K., Tsikerdekis, A., Amiridis, V., Marinou, E., Benedetti, A., Zanis, P., Alexandri,
1185 G., Mona, L., Kourtidis, K. A. and Lelieveld, J.: A 3-D evaluation of the MACC reanalysis dust
1186 product over Europe, northern Africa and Middle East using CALIOP/CALIPSO dust satellite
1187 observations, *Atmos. Chem. Phys.*, 18(12), 8601–8620, doi:10.5194/acp-18-8601-2018, 2018.
- 1188
- 1189 Giannakopoulou, E. M. and Toumi, R.: The Persian Gulf summertime low-level jet over sloping
1190 terrain, *Q. J. Roy. Meteor. Soc.*, 138, 145–157, doi:10.1002/qj.901, 2011.
- 1191
- 1192 Giglio, L., Randerson, J. T., and van der Werf, G. R.: Analysis of daily, monthly, and annual burned
1193 area using the fourth-generation global fire emissions database (GFED4), *J. Geophys. Res.-Biogeo.*,
1194 118, 317–328, 2013.
- 1195
- 1196 Giles, D. M., Holben, B. N., Eck, T. F., Sinyuk, A., Smirnov, A., Slutsker, I., Dickerson, R. R.,
1197 Thompson, A. M., and Schafer, J. S.: An analysis of AERONET aerosol absorption properties and
1198 classifications representative of aerosol source regions, *J. Geophys. Res.*, 117, D17203,
1199 <https://doi.org/10.1029/2012JD018127>, 2012.
- 1200
- 1201 Ginoux, P., Chin, M., Tegen, I., Prospero, J. M., Holben, B., Dubovik, O., and Lin, S. J.: Sources and
1202 distributions of dust aerosols simulated with the GOCART model, *J. Geophys. Res.-Atmos.*, 106,
1203 20255–20273, <https://doi.org/10.1029/2000jd000053>, 2001.
- 1204
- 1205 Ginoux, P., Prospero, J. M., Torres, O., and Chin, M.: Longterm simulation of global dust distribution
1206 with the GOCART model: correlation with North Atlantic Oscillation, *Environ. Modell. Softw.*, 19,
1207 113–128, [https://doi.org/10.1016/S1364-8152\(03\)00114-2](https://doi.org/10.1016/S1364-8152(03)00114-2), 2004.
- 1208



- 1209 Ginoux, P., Prospero, J. M., Gill, T. E., Hsu, N. C., and Zhao, M.: Global-scale attribution of
1210 anthropogenic and natural dust sources and their emission rates based on MODIS Deep Blue aerosol
1211 products, *Rev. Geophys.*, 50, RG3005, <https://doi.org/10.1029/2012RG000388>, 2012.
1212
- 1213 Gkikas, A., Hatzianastassiou, N., Mihalopoulos, N., Katsoulis, V., Kazadzis, S., Pey, J., Querol, X.,
1214 and Torres, O.: The regime of intense desert dust episodes in the Mediterranean based on
1215 contemporary satellite observations and ground measurements, *Atmos. Chem. Phys.*, 13, 12135-
1216 12154, <https://doi.org/10.5194/acp-13-12135-2013>, 2013.
1217
- 1218 Gkikas, A., Houssos, E. E., Lolis, C. J., Bartzokas, A., Mihalopoulos, N., and Hatzianastassiou, N.:
1219 Atmospheric circulation evolution related to desert-dust episodes over the Mediterranean, *Q. J. Roy.
1220 Meteor. Soc.*, 141, 1634–1645, doi:10.1002/qj.2466, 2015.
1221
- 1222 Gkikas, A., Basart, S., Hatzianastassiou, N., Marinou, E., Amiridis, V., Kazadzis, S., Pey, J., Querol,
1223 X., Jorba, O., Gassó, S., and Baldasano, J. M.: Mediterranean intense desert dust outbreaks and their
1224 vertical structure based on remote sensing data, *Atmos. Chem. Phys.*, 16, 8609-8642,
1225 <https://doi.org/10.5194/acp-16-8609-2016>, 2016.
1226
- 1227 Gkikas, A., Obiso, V., Pérez García-Pando, C., Jorba, O., Hatzianastassiou, N., Vendrell, L., Basart,
1228 S., Solomos, S., Gassó, S., and Baldasano, J. M.: Direct radiative effects during intense Mediterranean
1229 desert dust outbreaks, *Atmos. Chem. Phys.*, 18, 8757-8787, [https://doi.org/10.5194/acp-18-8757-](https://doi.org/10.5194/acp-18-8757-2018)
1230 2018, 2018.
1231
- 1232 Gkikas, A., Giannaros, T.M., Kotroni, V., Lagouvardos, K.: Assessing the radiative impacts of an
1233 extreme desert dust outbreak and the potential improvements on short-term weather forecasts: The
1234 case of February 2015, *Atmos. Res.*, 226, 152-170, <https://doi.org/10.1016/j.atmosres.2019.04.020>,
1235 2019.
1236
- 1237 Gong, S. L.: A parameterization of sea-salt aerosol source function for sub- and super-micron
1238 particles, *Global Biogeochem. Cy.*, 17, 1097, <https://doi.org/10.1029/2003GB002079>, 2003.
1239
- 1240 Hamidi, M., Kavianpour, M. R., and Shao, Y.: Synoptic analysis of dust storms in the Middle East,
1241 *Asia-Pac. J. Atmos. Sci.*, 49, 279–286, 2013.
1242



- 1243 Hand, J. L., White, W. H., Gebhart, K. A., Hyslop, N. P., Gill, T. E., and Schichtel, B. A.: Earlier
1244 onset of the spring fine dust season in the southwestern United States, *Geophys. Res. Lett.*, 43, 4001–
1245 4009, <https://doi.org/10.1002/2016gl068519>, 2016.
1246
- 1247 Hand, J. L., Gill, T. E., and Schichtel, B. A.: Spatial and seasonal variability in fine mineral dust and
1248 coarse aerosol mass at re-mote sites across the United States, *J. Geophys. Res.-Atmos.*, 122, 3080–
1249 3097, <https://doi.org/10.1002/2016jd026290>, 2017.
1250
- 1251 Haustein, K., Pérez, C., Baldasano, J. M., Jorba, O., Basart, S., Miller, R. L., Janjic, Z., Black, T.,
1252 Nickovic, S., Todd, M. C., Washington, R., Müller, D., Tesche, M., Weinzierl, B., Esselborn, M., and
1253 Schladitz, A.: Atmospheric dust modeling from meso to global scales with the online NMMB/BSC-
1254 Dust model – Part 2: Experimental campaigns in Northern Africa, *Atmos. Chem. Phys.*, 12, 2933–
1255 2958, <https://doi.org/10.5194/acp-12-2933-2012>, 2012.
1256
- 1257 Haywood, J. and Boucher, O.: Estimates of the direct and indirect radiative forcing due to
1258 tropospheric aerosols: A review, *Rev. Geophys.*, 38, 513–543,
1259 <https://doi.org/10.1029/1999RG000078>, 2000.
1260
- 1261 Hess, M., Koepke, P., and Schult, I.: Optical Properties of Aerosols and Clouds: The Software
1262 Package OPAC, *B. Am. Meteorol. Soc.*, 79, 831–844, [https://doi.org/10.1175/1520-0477\(1998\)0792.0.CO;2](https://doi.org/10.1175/1520-0477(1998)0792.0.CO;2), 1998.
1264
- 1265 Holben, B. N., Eck, T. F., Slutsker, I., Tanre, D., Buis, J. P., Setzer, A., Vermote, E., Reagan, J. A.,
1266 Kaufman, Y., Nakajima, T., Lavenue, F., Jankowiak, I., and Smirnov, A.: AERONET – A federated
1267 instrument network and data archive for aerosol characterization, *Remote Sens. Environ.*, 66, 1–16,
1268 [https://doi.org/10.1016/S0034-4257\(98\)00031-5](https://doi.org/10.1016/S0034-4257(98)00031-5), 1998.
1269
- 1270 Hsu, N. C., Tsay, S. C., King, M. D., and Herman, J. R.: Aerosol Properties Over Bright-Reflecting
1271 Source Regions, *IEEE T. Geosci. Remote*, 42, 557–569, doi:10.1109/TGRS.2004.824067, 2004.
1272
- 1273 Hubanks, P. A., Platnick, S., King, M., and Ridgway, R.: MODIS Atmosphere L3 Gridded Product
1274 Algorithm Theoretical Basis Document (ATBD) & Users Guide, ATBD Reference Number:
1275 L3_ATBD_C6_2018_04_11, 2018.
1276



- 1277 Huneus, N., Schulz, M., Balkanski, Y., Griesfeller, J., Prospero, J., Kinne, S., Bauer, S., Boucher,
1278 O., Chin, M., Dentener, F., Diehl, T., Easter, R., Fillmore, D., Ghan, S., Ginoux, P., Grini, A.,
1279 Horowitz, L., Koch, D., Krol, M. C., Landing, W., Liu, X., Mahowald, N., Miller, R., Morcrette, J.-
1280 J., Myhre, G., Penner, J., Perlwitz, J., Stier, P., Takemura, T., and Zender, C. S.: Global dust model
1281 intercomparison in AeroCom phase I, *Atmos. Chem. Phys.*, 11, 7781–7816,
1282 <https://doi.org/10.5194/acp-11-7781-2011>, 2011.
- 1283
- 1284 Hunt, W. H., Winker, D. M., Vaughan, M. A., Powell, K. A., Lucker, P. L. and Weimer, C.: CALIPSO
1285 Lidar Description and Performance Assessment, *J. Atmos. Oceanic Technol.*, 26(7), 1214–1228,
1286 [doi:10.1175/2009JTECHA1223.1](https://doi.org/10.1175/2009JTECHA1223.1), 2009.
- 1287
- 1288 Hussain, A., Mir, H., Afzal, M.: Analysis of dust storms frequency over Pakistan during (1961–2000),
1289 *Pakistan J. Meteorol.*, 2(3): 49–68, 2005.
- 1290
- 1291 Husar, R. B., Tratt, D. M., Schichtel, D. M., Falke, S. R., Li, F., Jaffe, D., Gassó, S., Gill, T.,
1292 Laulainen, N. S., Lu, F., Reheis, M. C., Chun, Y., Westphal, D., Holben, B. N., Gueymard, C., McK-
1293 endry, I., Kuring, N., Feldman, G. C., McClain, C., Frouin, R. J., Merrill, J., DuBois, D., Vignola, F.,
1294 Murayama, T., Nickovic, S., Wilson, W. E., Sassen, K., Sugimoto, N., and Malm, W. C.: Asian dust
1295 events of April 1998, *J. Geophys. Res.*, 106, 18317–18330, <https://doi.org/10.1029/2000JD900788>,
1296 2001.
- 1297
- 1298 Hyer, E. J., Reid, J. S., and Zhang, J.: An over-land aerosol optical depth data set for data assimilation
1299 by filtering, correction, and aggregation of MODIS Collection 5 optical depth retrievals, *Atmos.*
1300 *Meas. Tech.*, 4, 379-408, <https://doi.org/10.5194/amt-4-379-2011>, 2011.
- 1301
- 1302 Inness, A., Baier, F., Benedetti, A., Bouarar, I., Chabrillat, S., Clark, H., Clerbaux, C., Coheur, P.,
1303 Engelen, R. J., Errera, Q., Flemming, J., George, M., Granier, C., Hadji-Lazaro, J., Huijnen, V.,
1304 Hurtmans, D., Jones, L., Kaiser, J. W., Kapsomenakis, J., Lefever, K., Leitão, J., Razinger, M.,
1305 Richter, A., Schultz, M. G., Simmons, A. J., Suttie, M., Stein, O., Thépaut, J.-N., Thouret, V.,
1306 Vrekoussis, M., Zerefos, C., and the MACC team: The MACC reanalysis: an 8 yr data set of
1307 atmospheric composition, *Atmos. Chem. Phys.*, 13, 4073–4109, [https://doi.org/10.5194/acp13-4073-](https://doi.org/10.5194/acp13-4073-2013)
1308 2013, 2013.
- 1309
- 1310 Inness, A., Ades, M., Agustí-Panareda, A., Barré, J., Benedictow, A., Blechschmidt, A.-M.,
1311 Dominguez, J. J., Engelen, R., Eskes, H., Flemming, J., Huijnen, V., Jones, L., Kipling, Z., Massart,



- 1312 S., Parrington, M., Peuch, V.-H., Razinger, M., Remy, S., Schulz, M., and Suttie, M.: The CAMS
1313 reanalysis of atmospheric composition, *Atmos. Chem. Phys.*, 19, 3515–3556,
1314 <https://doi.org/10.5194/acp-19-3515-2019>, 2019.
- 1315
- 1316 Jickells, T. D., An, Z. S., Andersen, K. K., Baker, A. R., Bergametti, G., Brooks, N., Cao, J. J., Boyd,
1317 P. W., Duce, R. A., Hunter, K. A., Kawahata, H., Kubilay, N., laRoche, J., Liss, P. S., Mahowald, N.,
1318 Prospero, J. M., Ridgwell, A. J., Tegen, I., and Torres, R.: Global iron connections between desert
1319 dust, ocean biogeochemistry, and climate, *Science*, 308, 67–71, 2005.
- 1320
- 1321 Jickells, T., Boyd, P., and Hunter, K.: Biogeochemical impacts of dust on the global carbon cycle, in:
1322 *Mineral Dust*, edited by: Knippertz, P. and Stuut, J.-B. W., Springer, the Netherlands, 359–384, 2014.
- 1323
- 1324 Kanakidou, M., Mihalopoulos, N., Kindap, T., Im, U., Vrekoussis, M., Gerasopoulos, E., Dermizaki,
1325 E., Unal, A., Kocak, M., Markakis, K., Melas, D., Kouvarakis, G., Youssef, A. F., Richter, A.,
1326 Hatzianastassiou, N., Hilboll, A., Ebojje, F., Wittrock, F., von Savigny, C., Burrows, J. P.,
1327 Ladstaetter-Weissenmayer, A., and Moubasher, H.: Megacities as hot spots of air pollution in the
1328 East Mediterranean, *Atmos. Environ.*, 45, 1223–1235,
1329 <https://doi.org/10.1016/j.atmosenv.2010.11.048>, 2011.
- 1330
- 1331 Kanatani, K.T., Ito, I., Al-Delaimy, W.K., Adachi, Y., Mathews, W.C., Ramsdell, J.W.: Toyama
1332 Asian Desert Dust and Asthma Study Group Members. Desert dust exposure is associated with
1333 increased risk of asthma hospitalization in children, *Am. J. Respir. Crit. Care Med.* 182 (12),
1334 1475e1481. <https://doi.org/10.1164/rccm.201002-0296OC>, 2010.
- 1335
- 1336 Kanitz, T., Engelmann, R., Heinold, B., Baars, H., Skupin, A., and Ansmann, A.: Tracking the
1337 Saharan Air Layer with shipborne lidar across the tropical Atlantic, *Geophys. Res. Lett.*, 41, 1044–
1338 1050, doi:10.1002/2013GL058780, 2014.
- 1339
- 1340 Kaufman, Y. J., Koren, I., Remer, L. A., Tanré, D., Ginoux, P., and Fan, S.: Dust transport and
1341 deposition observed from the Terra-Moderate Resolution Imaging Spectroradiometer (MODIS)
1342 spacecraft over the Atlantic Ocean, *J. Geophys. Res.-Atmos.*, 110, 1–16,
1343 <https://doi.org/10.1029/2003JD004436>, 2005.
- 1344



- 1345 Kergoat, L., Guichard, F., Pierre, C., and Vassal, C.: Influence of dry-season vegetation variability
1346 on Sahelian dust during 2002–2015, *Geophys. Res. Lett.*, 44, 5231–5239,
1347 <https://doi.org/10.1002/2016GL072317>, 2017.
- 1348
- 1349 Kim, D., Chin, M., Yu, H., Eck, T. F., Sinyuk, A., Smirnov, A., and Holben, B. N.: Dust optical
1350 properties over North Africa and Arabian Peninsula derived from the AERONET dataset, *Atmos.*
1351 *Chem. Phys.*, 11, 10733-10741, <https://doi.org/10.5194/acp-11-10733-2011>, 2011.
- 1352
- 1353 Kittaka, C., Winker, D. M., Vaughan, M. A., Omar, A., and Remer, L. A.: Intercomparison of column
1354 aerosol optical depths from CALIPSO and MODIS-Aqua, *Atmos. Meas. Tech.*, 4, 131– 141,
1355 <https://doi.org/10.5194/amt-4-131-2011>, 2011.
- 1356
- 1357 Klingmüller, K., Pozzer, A., Metzger, S., Stenchikov, G. L., and Lelieveld, J.: Aerosol optical depth
1358 trend over the Middle East, *Atmos. Chem. Phys.*, 16, 5063-5073, [https://doi.org/10.5194/acp-16-](https://doi.org/10.5194/acp-16-5063-2016)
1359 5063-2016, 2016.
- 1360
- 1361 Klose, M. and Shao, Y.: Stochastic parameterization of dust emission and application to convective
1362 atmospheric conditions, *Atmos. Chem. Phys.*, 12, 7309-7320, [https://doi.org/10.5194/acp-12-7309-](https://doi.org/10.5194/acp-12-7309-2012)
1363 2012, 2012.
- 1364
- 1365 Knippertz, P., Deutscher, C., Kandler, K., Müller, T., Schulz, O., and Schütz, L.: Dust mobilization
1366 due to density currents in the Atlas region: Observations from the Saharan Mineral Dust Experiment
1367 2006 field campaign, *J. Geophys. Res.-Atmos.*, 112, 1–14, <https://doi.org/10.1029/2007JD008774>,
1368 2007.
- 1369
- 1370 Koch, J. and Renno, N. O.: The role of convective plumes and vortices on the global aerosol budget,
1371 *Geophys. Res. Lett.*, 32, L18806, doi:10.1029/2005GL023420, 2005.
- 1372
- 1373 Koch, D., Schulz, M., Kinne, S., McNaughton, C., Spackman, J. R., Balkanski, Y., Bauer, S.,
1374 Berntsen, T., Bond, T. C., Boucher, O., Chin, M., Clarke, A., De Luca, N., Dentener, F., Diehl, T.,
1375 Dubovik, O., Easter, R., Fahey, D. W., Feichter, J., Fillmore, D., Freitag, S., Ghan, S., Ginoux, P.,
1376 Gong, S., Horowitz, L., Iversen, T., Kirkevåg, A., Klimont, Z., Kondo, Y., Krol, M., Liu, X., Miller,
1377 R., Montanaro, V., Moteki, N., Myhre, G., Penner, J. E., Perlwitz, J., Pitari, G., Reddy, S., Sahu, L.,
1378 Sakamoto, H., Schuster, G., Schwarz, J. P., Seland, Ø., Stier, P., Takegawa, N., Takemura, T., Textor,



- 1379 C., van Aardenne, J. A., and Zhao, Y.: Evaluation of black carbon estimations in global aerosol
1380 models, *Atmos. Chem. Phys.*, 9, 9001-9026, <https://doi.org/10.5194/acp-9-9001-2009>, 2009.
- 1381
- 1382 Konsta, D., Biniotoglou, I., Gkikas, A., Solomos, S., Marinou, E., Proestakis, E., Basart, S., Pérez
1383 García-Pando, C., El-Askary, H., Amiridis, V.: Evaluation of the BSC-DREAM8b regional dust
1384 model using the 3D LIVAS-CALIPSO, *Atmos. Environ.*, 195, 46-62,
1385 <https://doi.org/10.1016/j.atmosenv.2018.09.047>, 2018.
- 1386
- 1387 Kosmopoulos, P. G., Kazadzis, S., Taylor, M., Athanasopoulou, E., Speyer, O., Raptis, P. I., Marinou,
1388 E., Proestakis, E., Solomos, S., Gerasopoulos, E., Amiridis, V., Bais, A. and Kontoes, C.: Dust impact
1389 on surface solar irradiance assessed with model simulations, satellite observations and ground-based
1390 measurements, *Atmos. Meas. Tech.*, 10(7), doi:10.5194/amt-10-2435-2017, 2017.
- 1391
- 1392 Kosmopoulos, P.G., Kazadzis, S., El-Askary, H., Taylor, M., Gkikas, A., Proestakis, E., Kontoes, C.,
1393 El-Khayat, M.M.: Earth-Observation-Based Estimation and Forecasting of Particulate Matter Impact
1394 on Solar Energy in Egypt, *Remote Sens.*, 10, 1870, 2018.
- 1395
- 1396 Lambert, F., Kug, J.-S., Park, R. J., Mahowald, N., Winckler, G., Abe-Ouchi, A., O'ishi, R.,
1397 Takemura, T., and Lee, J.-H.: The role of mineral-dust aerosols in polar temperature amplification,
1398 *Nat. Clim. Change*, 3, 487–491, <https://doi.org/10.1038/nclimate1785>, 2013.
- 1399
- 1400 Levy, R. C., Remer, L. A., and Dubovik, O.: Global aerosol optical properties and application to
1401 Moderate Resolution Imaging Spectroradiometer aerosol retrieval over land, *J. Geophys. Res.-*
1402 *Atmos.*, 112, D13210, doi:10.1029/2006JD007815, 2007a.
- 1403
- 1404 Levy, R. C., Remer, L. A., Mattoo, S., Vermote, E. F., and Kaufman, Y. J.: Second-generation
1405 operational algorithm: Retrieval of aerosol properties over land from inversion of Moderate
1406 Resolution Imaging Spectroradiometer spectral reflectance, *J. Geophys. Res.-Atmos.*, 112, D13211,
1407 doi:10.1029/2006JD007811, 2007b.
- 1408
- 1409 Levy, R. C., Leptoukh, G. G., Kahn, R., Zubko, V., Gopalan, A., and Remer, L. A.: A critical look at
1410 deriving monthly aerosol optical depth from satellite data, *IEEE Transactions on Geoscience and*
1411 *Remote Sensing*, 47, 2942–2956, <https://doi.org/10.1109/TGRS.2009.2013842>, 25 2009.
- 1412



- 1413 Levy, R. C., Remer, L. A., Kleidman, R. G., Mattoo, S., Ichoku, C., Kahn, R., and Eck, T. F.: Global
1414 evaluation of the Collection 5 MODIS dark-target aerosol products over land, *Atmos. Chem. Phys.*,
1415 10, 10399–10420, doi:10.5194/acp-10-10399-2010, 2010.
- 1416
- 1417 Levy, R. C., Mattoo, S., Munchak, L. A., Remer, L. A., Sayer, A. M., Patadia, F., and Hsu, N. C.:
1418 The Collection 6 MODIS aerosol products over land and ocean, *Atmos. Meas. Tech.*, 6, 2989–3034,
1419 <https://doi.org/10.5194/amt-6-2989-2013>, 2013.
- 1420
- 1421 Li, W., El-Askary, H., Qurban, M. A., Proestakis E., Garay M. J., Kalashnikova, O. V., Amiridis, V.,
1422 Gkikas, A., Marinou, E., Piechota, T. and ManiKandan, K. P.: An Assessment of Atmospheric and
1423 Meteorological Factors Regulating Red Sea Phytoplankton Growth, *Remote Sens.*, 10(5), 673;
1424 doi:10.3390/rs10050673, 2018.
- 1425
- 1426 Li, L., and Sokolik, I.: Analysis of Dust Aerosol Retrievals Using Satellite Data in Central Asia,
1427 *Atmosphere*, 9, 288, 2018.
- 1428
- 1429 Liu, D., Wang, Z., Liu, Z., Winker, D., and Trepte, C.: A height resolved global view of dust aerosols
1430 from the first year CALIPSO lidar measurements, *J. Geophys. Res.-Atmos.*, 113, D16214,
1431 <https://doi.org/10.1029/2007JD009776>, 2008.
- 1432
- 1433 Liu, D., Taylor, J. W., Crosier, J., Marsden, N., Bower, K. N., Lloyd, G., Ryder, C. L., Brooke, J. K.,
1434 Cotton, R., Marenco, F., Blyth, A., Cui, Z., Estelles, V., Gallagher, M., Coe, H., and Choulaton, T.
1435 W.: Aircraft and ground measurements of dust aerosols over the west African coast in summer 2015
1436 during ICE-D and AER-D, *Atmos. Chem. Phys.*, 18, 3817–3838, [https://doi.org/10.5194/acp-18-](https://doi.org/10.5194/acp-18-3817-2018)
1437 [3817-2018](https://doi.org/10.5194/acp-18-3817-2018), 2018.
- 1438
- 1439 Lynch, P., Reid, J. S., Westphal, D. L., Zhang, J., Hogan, T. F., Hyer, E. J., Curtis, C. A., Hegg, D.
1440 A., Shi, Y., Campbell, J. R., Rubin, J. I., Sessions, W. R., Turk, F. J., and Walker, A. L.: An 11-year
1441 global gridded aerosol optical thickness reanalysis (v1.0) for atmospheric and climate sciences,
1442 *Geosci. Model Dev.*, 9, 1489–1522, <https://doi.org/10.5194/gmd-9-1489-2016>, 2016.
- 1443
- 1444 Ma, X., Bartlett, K., Harmon, K., and Yu, F.: Comparison of AOD between CALIPSO and MODIS:
1445 significant differences over major dust and biomass burning regions, *Atmos. Meas. Tech.*, 6, 2391–
1446 2401, <https://doi.org/10.5194/amt-6-2391-2013>, 2013.
- 1447



- 1448 Mahowald, N. M. and Luo, C.: A less dusty future?, *Geophys. Res.Lett.*, 30, 1903,
1449 <https://doi.org/10.1029/2003GL017880>, 2003.
- 1450
- 1451 Mamouri, R. E. and Ansmann, A.: Fine and coarse dust separation with polarization lidar, *Atmos.*
1452 *Meas. Tech.*, 7, 3717-3735, <https://doi.org/10.5194/amt-7-3717-2014>, 2014.
- 1453
- 1454 Mamouri, R.-E. and Ansmann, A.: Potential of polarization/Raman lidar to separate fine dust, coarse
1455 dust, maritime, and anthropogenic aerosol profiles, *Atmos. Meas. Tech.*, 10(9), 3403–3427,
1456 [doi:10.5194/amt-10-3403-2017](https://doi.org/10.5194/amt-10-3403-2017), 2017.
- 1457
- 1458 Marinou, E., Amiridis, V., Biniotoglou, I., Tsikerdekis, A., Solomos, S., Proestakis, E., Konsta, D.,
1459 Papagiannopoulos, N., Tsekeri, A., Vlastou, G., Zanis, P., Balis, D., Wandinger, U., and Ansmann,
1460 A.: Three-dimensional evolution of Saharan dust transport towards Europe based on a 9-year
1461 EARLINET-optimized CALIPSO dataset, *Atmos. Chem. Phys.*, 17, 5893-5919,
1462 <https://doi.org/10.5194/acp-17-5893-2017>, 2017.
- 1463
- 1464 Marticoréna, B.: Mineral Dust - A key player in the Earth system, chap. Chapter 5: Dust production
1465 mechanisms, pp. 93–120, Springer, 2014.
- 1466
- 1467 McCarty, W., Coy, L., Gelaro, R., Huang, A., Merkova, D., Smith, E. B., Sienkiewicz, M., and
1468 Wargan, K.: MERRA-2 input observations: Summary and initial assessment. Technical Report Series
1469 on Global Modeling and Data Assimilation, Vol. 46, NASA Tech. Rep. NASA/TM–2016–104606,
1470 61 pp., 2016. [Available online at <https://gmao.gsfc.nasa.gov/pubs/docs/McCarty885.pdf>.]
- 1471
- 1472 Meng, Z. K., Yang, P., Kattawar, G. W., Bi, L., Liou, K. N., and Laszlo, I.: Single-scattering
1473 properties of tri-axial ellipsoidal mineral dust aerosols: A database for application to radiative transfer
1474 calculations, *J. Aerosol Sci.*, 41, 501–512, <https://doi.org/10.1016/j.jaerosci.2010.02.008>, 2010.
- 1475
- 1476 Middleton, H. J.: Desert dust hazards: A global review, *Aeolian Res.*, 24, 53–63, 2017.
- 1477
- 1478 Middleton, N. J. and Goudie, A. S.: Saharan dust: sources and trajectories, *T. I. Brit. Geogr.*, 26, 165–
1479 181, [doi:10.1111/1475-5661.00013](https://doi.org/10.1111/1475-5661.00013), 2001.
- 1480
- 1481 Middleton, N.J., Kang, U.: Sand and dust storms: impact mitigation, *Sustainability*, 9, 1053,
1482 <https://doi.org/10.3390/su9061053>, 2017.



1483

1484 Molod, A., Takacs, L., Suarez, M., and Bacmeister, J.: Development of the GEOS-5 atmospheric
1485 general circulation model: evolution from MERRA to MERRA2, *Geosci. Model Dev.*, 8, 1339-1356,
1486 <https://doi.org/10.5194/gmd-8-1339-2015>, 2015.

1487

1488 Mukkavilli, S.K., Prasad, A.A., Taylor, R.A., Huang, J., Troccoli, A., Kay, M.J.: Assessment of
1489 atmospheric aerosols from two reanalysis products over Australia, *Atmos. Res.*, 215, 149-164, 2019.

1490

1491 Müller, D., Ansmann, A., Mattis, I., Tesche, M., Wandinger, U., Althausen, D., and Pisani, G.:
1492 Aerosol-type-dependent lidar ratios observed with Raman lidar, *J. Geophys. Res.-Atmos.*, 112,
1493 <https://doi.org/10.1029/2006JD008292>, 2007.

1494

1495 Nabat, P., Somot, S., Mallet, M., Michou, M., Sevault, F., Driouech, F., Meloni, D., di Sarra, A., Di
1496 Biagio, C., Formenti, P., Sicard, M., Léon, J.-F., and Bouin, M.-N.: Dust aerosol radiative effects
1497 during summer 2012 simulated with a coupled regional aerosol–atmosphere–ocean model over the
1498 Mediterranean, *Atmos. Chem. Phys.*, 15, 3303-3326, <https://doi.org/10.5194/acp-15-3303-2015>,
1499 2015.

1500

1501 N'Tchayi Mbourou, G., Berrand, J. J., and Nicholson, S. E.: The diurnal and seasonal cycles of wind-
1502 borne dust over Africa north of the equator, *J. Appl. Meteorol.*, 36, 868–882, 1997.

1503

1504 Okin, G. S., Mahowald, N., Chadwick, O. A., and Artaxo, P.: Impact of desert dust on the
1505 biogeochemistry of phosphorus in terrestrial ecosystems, *Global Biogeochem. Cy.*, 18, GB2005,
1506 <https://doi.org/10.1029/2003GB002145>, 2004.

1507

1508 Omar, A. H., Winker, D. M., Vaughan, M. A., Hu, Y., Trepte, C. R., Ferrare, R. A., Lee, K. P.,
1509 Hostetler, C. A., Kittaka, C., Rogers, R. R., and Kuehn, R. E.: The CALIPSO Automated Aerosol
1510 Classification and Lidar Ratio Selection Algorithm, *J. Atmos. Ocean. Tech.*, 26, 1994–2014,
1511 <https://doi.org/10.1175/2009JTECHA1231.1>, 2009.

1512

1513 Omar, A. H., Winker, D. M., Tackett, J. L., Giles, D. M., Kar, J., Liu, Z., Vaughan, M. A., Powell,
1514 K. A., and Trepte, C. R., CALIOP and AERONET aerosol optical depth comparisons: One size fits
1515 none, *J. Geophys. Res.-Atmos.*, 118, 4748–4766, <https://doi.org/10.1002/jgrd.50330>, 2013.

1516



- 1517 O'Neill, N. T., Eck, T. F., Smirnov, A., Holben, B. N., and Thulasiraman, S.: Spectral discrimination
1518 of coarse and fine mode optical depth, *J. Geophys. Res.*, 108, 4559–4573,
1519 <https://doi.org/10.1029/2002JD002975>, 2003.
- 1520
- 1521 Paliwal, U., Sharma, M., and Burkhardt, J. F.: Monthly and spatially resolved black carbon emission
1522 inventory of India: uncertainty analysis, *Atmos. Chem. Phys.*, 16, 12457–12476,
1523 <https://doi.org/10.5194/acp-16-12457-2016>, 2016.
- 1524
- 1525 Pease, P. P., Tchakerian, V. P., and Tindale, N. W.: Aerosols over the Arabian Sea: geochemistry and
1526 source areas for Aeolian desert dust, *J. Arid Environ.*, 39, 477–496,
1527 <https://doi.org/10.1006/jare.1997.0368>, 1998.
- 1528
- 1529 Pérez, C., Nickovic, S., Pejanovic, G., Baldasano, J. M., and Özsoy, E.: Interactive dust-radiation
1530 modeling: A step to improve weather forecasts, *J. Geophys. Res.*, 111, 1–17, 2006.
- 1531
- 1532 Pérez, C., Haustein, K., Janjic, Z., Jorba, O., Huneus, N., Baldasano, J. M., Black, T., Basart, S.,
1533 Nickovic, S., Miller, R. L., Perlwitz, J. P., Schulz, M., and Thomson, M.: Atmospheric dust modeling
1534 from meso to global scales with the online NMMB/BSC-Dust model – Part 1: Model description,
1535 annual simulations and evaluation, *Atmos. Chem. Phys.*, 11, 13001–13027,
1536 <https://doi.org/10.5194/acp-11-13001-2011>, 2011.
- 1537
- 1538 Pérez García-Pando, C., Stanton, M. C., Diggle, P. J., Trzaska, S., Miller, R. L., Perlwitz, J. P.,
1539 Baldasano, J. M., Cuevas, E., Ceccato, P., Yaka, P., and Thomson, M. C.: Soil Dust Aerosols and
1540 Wind as Predictors of Seasonal Meningitis Incidence in Niger, *Environ. Health Perspect.*, 122, 679–
1541 686, [doi:10.1289/ehp.1306640](https://doi.org/10.1289/ehp.1306640), 2014.
- 1542
- 1543 Peyridieu, S., Chédin, A., Capelle, V., Tsamalis, C., Pierangelo, C., Armante, R., Crevoisier, C.,
1544 Crépeau, L., Siméon, M., Ducos, F., and Scott, N. A.: Characterisation of dust aerosols in the infrared
1545 from IASI and comparison with PARASOL, MODIS, MISR, CALIOP, and AERONET observations,
1546 *Atmos. Chem. Phys.*, 13, 6065–6082, <https://doi.org/10.5194/acp-13-6065-2013>, 2013.
- 1547
- 1548 Proestakis, E., Amiridis, V., Marinou, E., Georgoulas, A. K., Solomos, S., Kazadzis, S., Chimot, J.,
1549 Che, H., Alexandri, G., Binietoglou, I., Daskalopoulou, V., Kourtidis, K. A., de Leeuw, G., and van
1550 der A, R. J.: Nine-year spatial and temporal evolution of desert dust aerosols over South and East



- 1551 Asia as revealed by CALIOP, *Atmos. Chem. Phys.*, 18, 1337-1362, [https://doi.org/10.5194/acp-18-](https://doi.org/10.5194/acp-18-1337-2018)
1552 1337-2018, 2018.
- 1553
- 1554 Prospero, J. M.: Saharan dust transport over the north Atlantic Ocean and Mediterranean: An
1555 Overview, in *The Impact of Desert Dust from Northern Africa Across the Mediterranean*, Springer,
1556 Dordrecht, <https://doi.org/10.1007/978-94-017-3354-0>, 1996.
- 1557
- 1558 Prospero, J. M.: Long-range transport of mineral dust in the global atmosphere: Impact of African
1559 dust on the environment of the southeastern United States, *P. Natl. Acad. Sci. USA*, 96, 3396–3403,
1560 1999.
- 1561
- 1562 Prospero, J. M., Collard, F. X., Molinie, J., and Jeannot, A.: Characterizing the annual cycle of
1563 African dust transport to the Caribbean Basin and South America and its impact on the environment
1564 and air quality, *Global Biogeochem. Cy.*, 28, 757–773, <https://doi.org/10.1002/2013gb004802>, 2014.
- 1565
- 1566 Prospero, J. M., Ginoux, P., Torres, O., Nicholson, S. E., and Gill, T. E.: Environmental
1567 characterization of global sources of atmospheric soil dust identified with the Nimbus 7 Total Ozone
1568 Mapping Spectrometer (TOMS) absorbing aerosol product, *Rev. Geophys.*, 40, 2-1–2-31, 2002.
- 1569
- 1570 Prospero, J. M. and Lamb, P. J.: African droughts and dust transport to the Caribbean: climate change
1571 implications, *Science*, 302, 1024–1027, doi:10.1126/science.1089915, 2003.
- 1572
- 1573 Prospero, J. M. and Mayol-Bracero, O. L.: Understanding the transport and impact of African dust
1574 on the Caribbean Basin, *B. Am. Meteorol. Soc.*, 94, 1329–1335, 2013.
- 1575
- 1576 Ramaswamy, V.P., Muraleedharan, M., Prakash Babu, C.: Mid-troposphere transport of Middle-East
1577 dust over the Arabian Sea and its effect on rainwater composition and sensitive ecosystems over India.
1578 *Scientific Reports* 7, 13676, <https://doi.org/10.1038/s41598-017-13652-1>, 2018.
- 1579
- 1580 Randerson, J. T., Chen, Y., Werf, G. R., Rogers, B. M., and Morton, D. C.: Global burned area and
1581 biomass burning emissions from small fires, *J. Geophys. Res.-Biogeo.*, 117, G04012,
1582 <https://doi.org/10.1029/2012JG002128>, 2012.



- 1583 Rashki, A., Kaskaoutis, D.G., Francois, P., Kosmopoulos, P.G., Legrand, M.: Dust-storm dynamics
1584 over Sistan region, Iran: seasonality, transport characteristics and affected areas, *Aeol. Res.*, 16, 35–
1585 48, 2015.
- 1586 Reid, J. S., Reid, E. A., Walker, A., Piketh, S., Cliff, S., Al Mandoos, A., Tsay, S.-C., and Eck, T. F.:
1587 Dynamics of southwest Asian dust particle size characteristics with implications for global dust
1588 research, *J. Geophys. Res.*, 113, D14212, <https://doi.org/10.1029/2007JD009752>, 2008.
1589
- 1590 Remer, L. A., Tanre, D., Kaufman, Y. J., Ichoku, C., Mattoo, S., Levy, R., Chu, D. A., Holben, B.,
1591 Dubovik, O., Smirnov, A., Martins, J. V., Li, R. R., and Ahmad, Z.: Validation of MODIS aerosol
1592 retrieval over ocean, *Geophys. Res. Lett.*, 29, MOD3.1–MOD3.4, doi:10.1029/2001GL013204, 2002.
1593
- 1594 Remer, L. A., Kaufman, Y. J., Tanre, D., Mattoo, S., Chu, D. A., Martins, J. V., Li, R. R., Ichoku, C.,
1595 Levy, R. C., Kleidman, R. G., Eck, T. F., Vermote, E., and Holben, B. N.: The MODIS aerosol
1596 algorithm, products, and validation, *J. Atmos. Sci.*, 62, 947–973, doi:10.1175/JAS3385.1, 2005.
1597
- 1598 Remer, L. A., Kleidman, R. G., Levy, R. C., Kaufman, Y. J., Tanré, D., Mattoo, S., Martins, J. V.,
1599 Ichoku, C., Koren, I., Yu, H. and Holben, B. N.: Global aerosol climatology from the MODIS satellite
1600 sensors, *J. Geophys. Res.-Atmos.*, 113, D14S07, doi:10.1029/2007JD009661, 2008.
1601
- 1602 Ridley, D. A., Heald, C. L., Kok, J. F., and Zhao, C.: An observationally constrained estimate of
1603 global dust aerosol optical depth, *Atmos. Chem. Phys.*, 16, 15097–15117,
1604 <https://doi.org/10.5194/acp-16-15097-2016>, 2016.
1605
- 1606 Rienecker, M. M., Suarez, M. J., Todling, R., Bacmeister, J., Takacs, L., Liu, H. C., Gu, W.,
1607 Sienkiewicz, M., Koster, R. D., Gelaro, R., Stajner, I., and Nielsen, J. E.: The GEOS-5 Data
1608 Assimilation System-Documentation of Versions 5.0.1, 5.1.0, and 5.2.0 Technical Report Series on
1609 Global Modeling and Data Assimilation, v27, 2008.
1610
- 1611 Rodríguez, S., Alastuey, A., and Querol, X.: A review of methods for long term in situ
1612 characterization of aerosol dust, *Aeolian Res.*, 6, 55–74, doi:10.1016/j.aeolia.2012.07.004, 2012.
1613
- 1614 Sayer, A. M., Hsu, N. C., Bettenhausen, C., and Jeong, M.-J.: Validation and uncertainty estimates
1615 for MODIS Collection 6 “Deep Blue” aerosol data, *J. Geophys. Res.*, 118, 7864–7873,
1616 <https://doi.org/10.1002/jgrd.50600>, 2013.



1617

1618 Sayer, A. M., Munchak, L. A., Hsu, N. C., Levy, R. C., Bettenhausen, C., and Jeong, M.-J.: MODIS
1619 Collection 6 aerosol products: comparison between aqua's e-deep blue, dark target, and "merged"
1620 data sets, and usage recommendations, *J. Geophys. Res.-Atmos.*, 119, 13965–13989,
1621 doi:10.1002/2014JD022453, 2014.

1622

1623 Schepanski, K.: Transport of Mineral Dust and Its Impact on Climate, *Geosciences*, 8,
1624 <https://doi.org/10.3390/geosciences8050151>, 2018.

1625

1626 Schepanski, K., Heinold, B., and Tegen, I.: Harmattan, Saharan heat low, and West African monsoon
1627 circulation: modulations on the Saharan dust outflow towards the North Atlantic, *Atmos. Chem.
1628 Phys.*, 17, 10223-10243, <https://doi.org/10.5194/acp-17-10223-2017>, 2017.

1629

1630 Schuster, G. L., Vaughan, M., MacDonnell, D., Su, W., Winker, D., Dubovik, O., Lapyonok, T., and
1631 Trepte, C.: Comparison of CALIPSO aerosol optical depth retrievals to AERONET measurements,
1632 and a climatology for the lidar ratio of dust, *Atmos. Chem. Phys.*, 12, 7431-7452,
1633 <https://doi.org/10.5194/acp-12-7431-2012>, 2012.

1634

1635 Shi, Y., Zhang, J., Reid, J. S., Holben, B., Hyer, E. J., and Curtis, C.: An analysis of the collection 5
1636 MODIS over-ocean aerosol optical depth product for its implication in aerosol assimilation, *Atmos.
1637 Chem. Phys.*, 11, 557-565, <https://doi.org/10.5194/acp-11-557-2011>, 2011.

1638

1639 Sokolik, I. N. and Toon, O. B.: Direct radiative forcing by anthropogenic airborne mineral aerosols,
1640 *Nature*, 381, 681–683, <https://doi.org/10.1038/381681a0>, 1996.

1641

1642 Solomos, S., Kalivitis, N., Mihalopoulos, N., Amiridis, V., Kouvarakis, G., Gkikas, A., Biniotoglou,
1643 I., Tsekeri, A., Kazadzis, S., Kottas, M., Pradhan, Y., Proestakis, E., Nastos, P. T. and Marengo, F.:
1644 From Tropospheric Folding to Khamsin and Foehn Winds: How Atmospheric Dynamics Advanced
1645 a Record-Breaking Dust Episode in Crete, *Atmosphere*, 9(7), 240, doi:10.3390/atmos9070240, 2018.

1646

1647 Stefanski, R. and Sivakumar, M. V. K.: Impacts of sand and dust storms on agriculture and potential
1648 agricultural applications of a SDSWS, *IOP Conf. Ser.: Earth Environ. Sci.*, 7, 012016, doi:
1649 10.1088/1755-1307/7/1/012016, 2009.

1650



- 1651 Stephens, G. L., Vane, D. G., Boain, R. J., Mace, G. G., Sassen, K., Wang, Z. E., Illingworth, A. J.,
1652 O'Connor, E. J., Rossow, W. B., Durden, S. L., Miller, S. D., Austin, R. T., Benedetti, A. and
1653 Mitrescu, C.: The cloudsat mission and the a-train - A new dimension of space-based observations of
1654 clouds and precipitation, *Bull. Amer. Meteorol. Soc.*, 83(12), 1771–1790, doi:10.1175/BAMS-83-
1655 12-1771, 2002.
- 1656
- 1657 Su, L. and Toon, O. B.: Saharan and Asian dust: similarities and differences determined by CALIPSO,
1658 AERONET, and a coupled climate-aerosol microphysical model, *Atmos. Chem. Phys.*, 11, 3263-
1659 3280, <https://doi.org/10.5194/acp-11-3263-2011>, 2011.
- 1660
- 1661 Sun, Y., Chen, H., Tada, R., Weiss, D., Lin, M., Toyoda, S., Yan, Y., and Isozaki, Y.: ESR signal
1662 intensity and crystallinity of quartz from Gobi and sandy deserts in East Asia and implication for
1663 tracing Asian dust provenance, *Geochem. Geophys. Geosy.*, 14, 2615–2627,
1664 <https://doi.org/10.1002/ggge.20162>, 2013.
- 1665
- 1666 Sun, E., Xu, X., Che, H., Tang, Z., Gui, K., An, L., Lu, C., and Shi, G.: Variation in MERRA-2
1667 aerosol optical depth and absorption aerosol optical depth over China from 1980 to 2017, *J. Atmos.*
1668 *Sol.-Terr. Phys.*, 186, 8–19, <https://doi.org/10.1016/j.jastp.2019.01.019>, 2019.
- 1669
- 1670 Tackett, J. L., Winker, D. M., Getzewich, B. J., Vaughan, M. A., Young, S. A. and Kar, J.: CALIPSO
1671 lidar level 3 aerosol profile product: version 3 algorithm design, *Atmos. Meas. Tech.*, 11(7), 4129–
1672 4152, doi:10.5194/amt-11-4129-2018, 2018.
- 1673
- 1674 Tafuro, A. M., Barnaba, F., De Tomasi, F., Perrone, M. R., and Gobbi, G. P.: Saharan dust particle
1675 properties over the central Mediterranean, *Atmos. Res.*, 81, 67–93, 2006.
- 1676
- 1677 Tesche, M., Ansmann, A., Müller, D., Althausen, D., Engelmann, R., Freudenthaler, V., and Grob,
1678 S.: Vertically Resolved Separation of Dust and Smoke over Cape Verde Using Multiwavelength
1679 Raman and Polarization Lidars during Saharan Mineral Dust Experiment 2008, *J. Geophys. Res.*,
1680 114, D13202, doi:10.1029/2009JD011862, 2009.
- 1681
- 1682 Textor, C., Schulz, M., Guibert, S., Kinne, S., Balkanski, Y., Bauer, S., Berntsen, T., Berglen, T.,
1683 Boucher, O., Chin, M., Dentener, F., Diehl, T., Easter, R., Feichter, H., Fillmore, D., Ghan, S.,
1684 Ginoux, P., Gong, S., Grini, A., Hendricks, J., Horowitz, L., Huang, P., Isaksen, I., Iversen, I., Kloster,
1685 S., Koch, D., Kirkevåg, A., Kristjansson, J. E., Krol, M., Lauer, A., Lamarque, J. F., Liu, X.,



- 1686 Montanaro, V., Myhre, G., Penner, J., Pitari, G., Reddy, S., Seland, Ø., Stier, P., Takemura, T., and
1687 Tie, X.: Analysis and quantification of the diversities of aerosol life cycles within AeroCom, *Atmos.*
1688 *Chem. Phys.*, 6, 1777-1813, <https://doi.org/10.5194/acp-6-1777-2006>, 2006.
- 1689
- 1690 Toledano, C., Cachorro, V. E., Berjon, A., De Frutos, A. M., Sorribas, M., De la Morena, B. A., and
1691 Goloub, P.: Aerosol optical depth and Ångström exponent climatology at El Arenosillo AERONET
1692 site (Huelva, Spain), *Q. J. Roy. Meteor. Soc.*, 133, 795–807, 2007.
- 1693
- 1694 Torres, O., Bhartia, P. K., Jethva, H., and Ahn, C.: Impact of the ozone monitoring instrument row
1695 anomaly on the long-term record of aerosol products, *Atmos. Meas. Tech.*, 11, 2701-2715,
1696 <https://doi.org/10.5194/amt-11-2701-2018>, 2018.
- 1697
- 1698 Tsikerdekis, A., Zanis, P., Steiner, A. L., Solmon, F., Amiridis, V., Marinou, E., Katragkou, E.,
1699 Karacostas, T., and Foret, G.: Impact of dust size parameterizations on aerosol burden and radiative
1700 forcing in RegCM4, *Atmos. Chem. Phys.*, 17, 769–791, <https://doi.org/10.5194/acp-17-769-2017>,
1701 2017.
- 1702
- 1703 van der Werf, G. R., Randerson, J. T., Giglio, L., Collatz, G. J., Kasibhatla, P. S., and Arellano Jr.,
1704 A. F.: Interannual variability in global biomass burning emissions from 1997 to 2004, *Atmos. Chem.*
1705 *Phys.*, 6, 3423-3441, <https://doi.org/10.5194/acp-6-3423-2006>, 2006.
- 1706
- 1707 Vaughan, M. A., Powell, K. A., Kuehn, R. E., Young, S. A., Winker, D. M., Hostetler, C. A., Hunt,
1708 W. H., Liu, Z., McGill, M. J. and Getzewich, B. J.: Fully Automated Detection of Cloud and Aerosol
1709 Layers in the CALIPSO Lidar Measurements, *J. Atmos. Ocean. Technol.*, 26(10), 2034–2050,
1710 [doi:10.1175/2009JTECHA1228.1](https://doi.org/10.1175/2009JTECHA1228.1), 2009.
- 1711
- 1712 Veselovskii, I., Goloub, P., Podvin, T., Tanre, D., da Silva, A., Colarco, P., Castellanos, P.,
1713 Korenskiy, M., Hu, Q., Whiteman, D. N., Pérez-Ramírez, D., Augustin, P., Fourmentin, M., and
1714 Kolgotin, A.: Characterization of smoke and dust episode over West Africa: comparison of MERRA-
1715 2 modeling with multiwavelength Mie–Raman lidar observations, *Atmos. Meas. Tech.*, 11, 949-969,
1716 <https://doi.org/10.5194/amt-11-949-2018>, 2018.
- 1717



- 1718 Vickery, K. J., Eckardt, F. D., and Bryant, R. G.: A sub-basin scale dust plume source frequency
1719 inventory for south-ern Africa, 2005–2008, *Geophys. Res. Lett.*, 40, 5274–5279,
1720 doi:10.1002/grl.50968, 2013.
- 1721
- 1722 Voss, K. K., and Evan, A. T.: A new satellite-based global climatology of dust aerosol optical depth.
1723 *Journal of Applied Meteorology and Climatology*, doi:10.1175/jamc-d-19-0194.1, 2020.
- 1724
- 1725 Wandinger, U., Tesche, M., Seifert, P., Ansmann, A., Müller, D., and Althausen, D.: Size matters:
1726 Influence of multiple scattering on CALIPSO light-extinction profiling in desert dust, *Geophys. Res.*
1727 *Lett.*, 37, L10801, doi:10.1029/2010GL042815, 2010.
- 1728 Washington, R., Todd, M., Middleton, N. J., and Goudie, A. S.: Dust-storm source areas determined
1729 by the total ozone monitoring spectrometer and surface observations, *Ann. Assoc. Am. Geogr.*, 93,
1730 297–313, <https://doi.org/10.1111/1467-8306.9302003>, 2003.
- 1731
- 1732 Wei, J., Peng, Y., Mahmood, R., Sun, L., and Guo, J.: Intercomparison in spatial distributions and
1733 temporal trends derived from multi-source satellite aerosol products, *Atmos. Chem. Phys.*, 19, 7183–
1734 7207, <https://doi.org/10.5194/acp-19-7183-2019>, 2019.
- 1735
- 1736 Weinzierl, B., Sauer, D., Minikin, A., Reitebuch, O., Dahlkötter, F., Mayer, B., Emde, C., Tegen, I.,
1737 Gasteiger, J., Petzold, A., Veira, A., Kueppers, U., and Schumann, U.: On the visibility of airborne
1738 volcanic ash and mineral dust from the pilot's perspective in flight, *Phys Chem Earth*, 45-46, 87-102,
1739 10.1016/j.pce.2012.04.003, 2012.
- 1740
- 1741 Winker, D. M., Pelon, J., Coakley, J. A., Ackerman, S. A., Charlson, R. J., Colarco, P. R., Flamant,
1742 P., Fu, Q., Hoff, R. M., Kittaka, C., Kubar, T. L., Le Treut, H., McCormick, M. P., Megie, G., Poole,
1743 L., Powell, K., Trepte, C., Vaughan, M. A. and Wielicki, B. A.: THE CALIPSO MISSION A Global
1744 3D View of Aerosols and Clouds, *Bull. Amer. Meteorol. Soc.*, 91(9), 1211–1229,
1745 doi:10.1175/2010BAMS3009.1, 2010.
- 1746
- 1747 Winker, D. M., Vaughan, M. A., Omar, A., Hu, Y., Powell, K. A., Liu, Z., Hunt, W. H. and Young,
1748 S. A.: Overview of the CALIPSO Mission and CALIOP Data Processing Algorithms, *J. Atmos.*
1749 *Oceanic Technol.*, 26(11), 2310–2323, doi:10.1175/2009JTECHA1281.1, 2009.
- 1750



- 1751 Wu, W. S., Purser, R. J., and Parrish, D. F.: Three-dimensional variational analysis with spatially
1752 inhomogeneous covariances, *Mon. Weather Rev.*, 130, 2905–2916, doi:10.1175/1520-
1753 0493(2002)1302.0.Co;2, 2002.
- 1754
- 1755 Yu, H. B., Chin, M., Winker, D. M., Omar, A. H., Liu, Z. Y., Kittaka, C., and Diehl, T.: Global view
1756 of aerosol vertical distributions from CALIPSO lidar measurements and GOCART simulations:
1757 Regional and seasonal variations, *J. Geophys. Res.-Atmos.*, 115, D00H30,
1758 <https://doi.org/10.1029/2009jd013364>, 2010.
- 1759
- 1760 Yu, H. B., Chin, M., Yuan, T. L., Bian, H. S., Remer, L. A., Prospero, J. M., Omar, A., Winker, D.,
1761 Yang, Y. K., Zhang, Y., Zhang, Z. B., and Zhao, C.: The fertilizing role of African dust in the Amazon
1762 rainforest: A first multiyear assessment based on data from Cloud-Aerosol Lidar and Infrared
1763 Pathfinder Satellite Observations, *Geophys. Res. Lett.*, 42, 1984–1991,
1764 <https://doi.org/10.1002/2015gl063040>, 2015.
- 1765
- 1766 Yu, Y., Kalashnikova, O. V., Garay, M. J., and Notaro, M.: Climatology of Asian dust activation and
1767 transport potential based on MISR satellite observations and trajectory analysis, *Atmos. Chem. Phys.*,
1768 19, 363–378, <https://doi.org/10.5194/acp-19-363-2019>, 2019.
- 1769
- 1770 Yu, Y., Notaro, M., Liu, Z., Kalashnikova, O., Alkolibi, F., Fadda, E., and Bakhrjy, F.: Assessing
1771 temporal and spatial variations in atmospheric dust over Saudi Arabia through satellite, radiometric,
1772 and station data, *J. Geophys. Res.-Atmos.*, 118, 13253– 13264,
1773 <https://doi.org/10.1002/2013JD020677>, 2013.
- 1774
- 1775 Yu, H., Remer, L. A., Chin, M., Bian, H., Kleidman, R. G., and Diehl, T.: A satellite-based assessment
1776 of transpacific transport of pollution aerosol, *J. Geophys. Res.-Atmos.*, 113, D14S12,
1777 <https://doi.org/10.1029/2007JD009349>, 2008.
- 1778
- 1779 Zender, C. S., Huisheng, B., and Newman, D.: Mineral Dust Entrainment and Deposition (DEAD)
1780 model: Description and 1990s dust climatology, *J. Geophys. Res.*, 108, 4416,
1781 <https://doi.org/10.1029/2002JD002775>, 2003.
- 1782
- 1783 Zender, C. S., Miller, R. L. L., and Tegen, I.: Quantifying mineral dust mass budgets: Terminology,
1784 constraints, and current estimates, *Eos, Transactions American Geophysical Union*, 85, 509–512,
1785 <https://doi.org/10.1029/2004EO480002>, 2011.



1786

1787 Zhang, J. and Reid, J. S.: MODIS aerosol product analysis for data assimilation: Assessment of over-
1788 ocean level 2 aerosol optical thickness retrievals, *J. Geophys. Res.-Atmos.*, 111, D22207,
1789 <https://doi.org/10.1029/2005JD006898>, 2006.

1790

1791 Zhang, R., Wang, G., Guo, S., Zamora, M. L., Ying, Q., Lin, Y., Wang, W., Hu, M., and Wang, Y.:
1792 Formation of urban fine particulate matter, *Chem. Rev.*, 115, 3803–3855, 2015.

1793

1794

1795

1796

1797

1798

1799

1800

1801

1802

1803

1804

1805

1806

1807

1808

1809

1810

1811

1812

1813

1814

1815

1816

1817

1818

1819

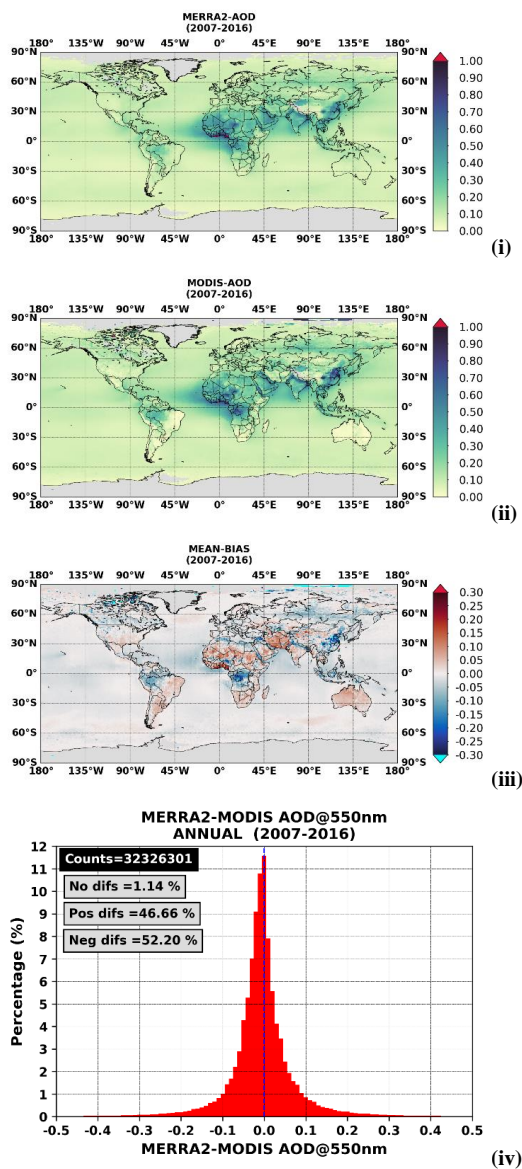
1820



1821 **Table 1:** Planetary (GLB), hemispherical (NHE and SHE) and regional DOD averages, representative for the period
 1822 2007-2015, based on collocated CALIOP, MERRA-2 and MIDAS 1°x1° data. Within the brackets are given the minimum
 1823 and maximum limits. The regional averages have been calculated following the upper branch (first temporal averaging
 1824 and then spatial averaging) in Figure 5 of Levy et al. (2009). The full names of the acronyms for each sub-region are
 1825 given in the caption of Figure S7.
 1826

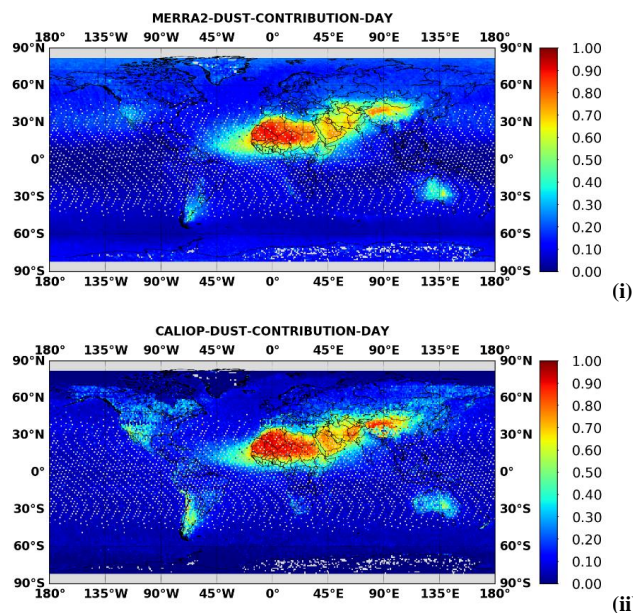
| REGION | CALIOP | MERRA-2 | MIDAS |
|--------|---------------------|---------------------|---------------------|
| GLB | 0.029 [0.027-0.033] | 0.031 [0.027-0.035] | 0.031 [0.028-0.035] |
| NHE | 0.050 [0.048-0.062] | 0.055 [0.049-0.065] | 0.055 [0.051-0.065] |
| SHE | 0.008 [0.007-0.008] | 0.007 [0.006-0.008] | 0.007 [0.006-0.008] |
| ETA | 0.105 [0.083-0.172] | 0.095 [0.077-0.141] | 0.108 [0.086-0.163] |
| WTA | 0.027 [0.022-0.034] | 0.019 [0.016-0.024] | 0.021 [0.018-0.028] |
| MED | 0.072 [0.062-0.092] | 0.089 [0.079-0.102] | 0.091 [0.082-0.107] |
| GOG | 0.166 [0.085-0.292] | 0.275 [0.076-0.434] | 0.323 [0.097-0.488] |
| WSA | 0.259 [0.233-0.332] | 0.337 [0.309-0.388] | 0.306 [0.275-0.393] |
| SSA | 0.291 [0.237-0.397] | 0.263 [0.158-0.356] | 0.253 [0.163-0.355] |
| BOD | 0.309 [0.217-0.366] | 0.519 [0.393-0.637] | 0.598 [0.416-0.883] |
| NME | 0.218 [0.104-0.257] | 0.243 [0.142-0.252] | 0.296 [0.144-0.350] |
| SME | 0.212 [0.171-0.253] | 0.203 [0.176-0.258] | 0.186 [0.156-0.237] |
| CAS | 0.078 [0.051-0.090] | 0.139 [0.128-0.202] | 0.137 [0.106-0.184] |
| THA | 0.172 [0.112-0.204] | 0.143 [0.113-0.156] | 0.137 [0.079-0.155] |
| TAK | 0.372 [0.284-0.448] | 0.262 [0.234-0.320] | 0.144 [0.102-0.285] |
| GOB | 0.121 [0.090-0.156] | 0.120 [0.107-0.147] | 0.154 [0.073-0.146] |
| EAS | 0.089 [0.055-0.131] | 0.065 [0.049-0.080] | 0.077 [0.060-0.094] |
| WNP | 0.015 [0.013-0.019] | 0.026 [0.021-0.029] | 0.027 [0.022-0.030] |
| ENP | 0.008 [0.005-0.011] | 0.018 [0.014-0.019] | 0.018 [0.015-0.022] |
| SUS | 0.021 [0.011-0.031] | 0.028 [0.016-0.040] | 0.027 [0.012-0.042] |

1827
 1828
 1829
 1830
 1831

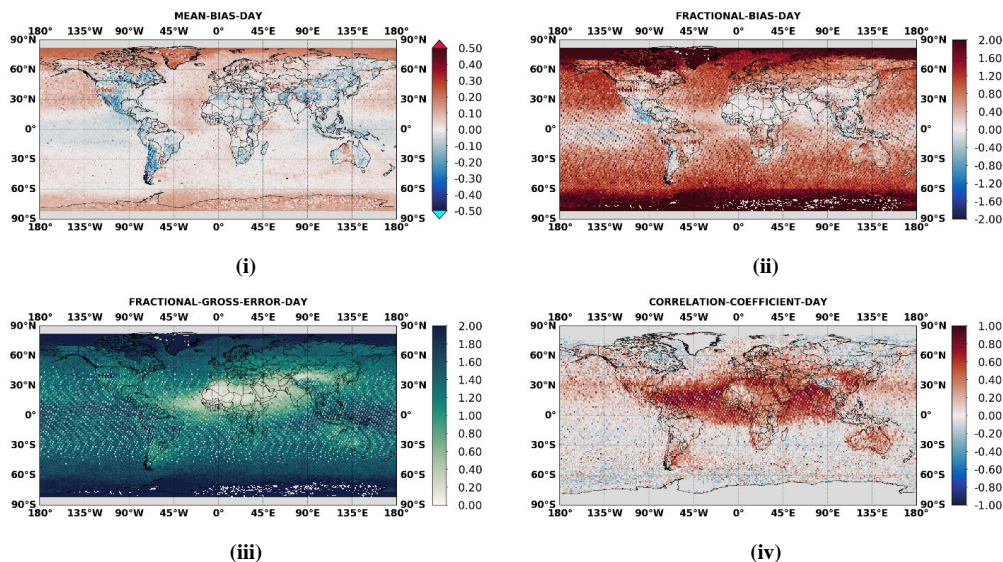


1832 **Figure 1:** Annual geographical distributions of: (i) MERRA-2 AOD_{550nm}, (ii) MODIS-Aqua AOD_{550nm} and (iii)
1833 MERRA2-MODIS AOD_{550nm} biases, at 1° x 1° spatial resolution, averaged over the period 2007 – 2016. (iv) Relative
1834 frequency histogram of MERRA2-MODIS AOD_{550nm} differences.

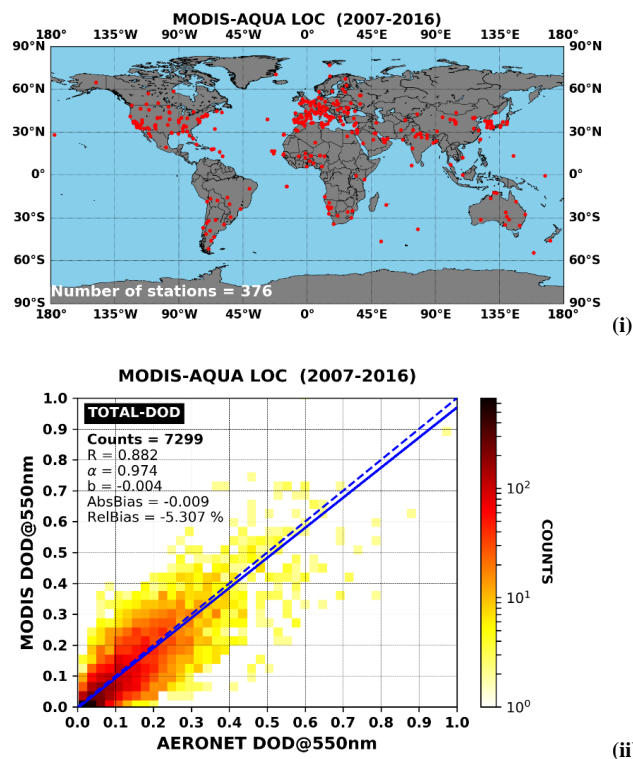
1835



1836 **Figure 2:** Annual geographical distributions of dust contribution to total aerosol optical depth, at $1^\circ \times 1^\circ$ spatial resolution,
1837 based on: (i) MERRA-2 products at 550 nm and (ii) CALIOP retrievals at 532 nm, during daytime conditions, over the
1838 period 2007-2015.
1839

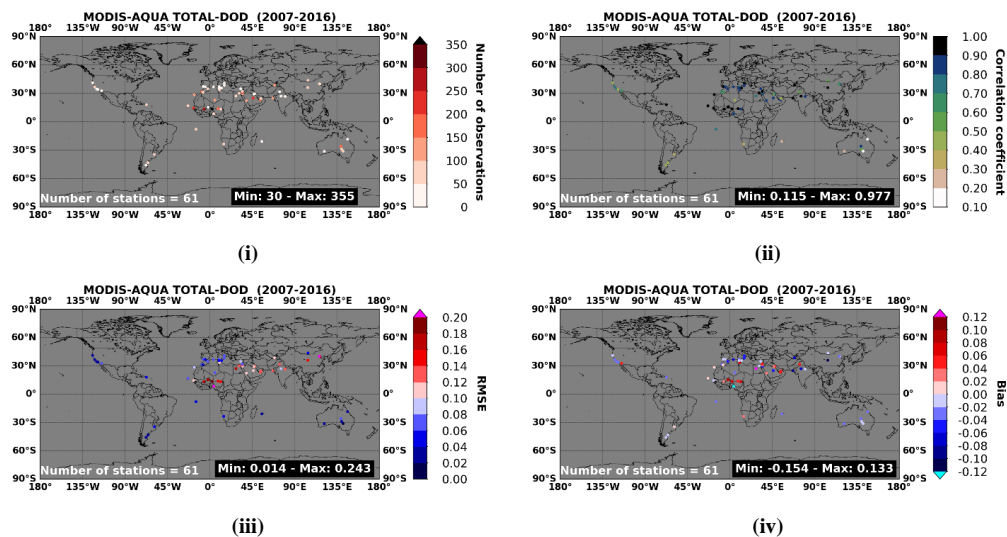


1840 **Figure 3:** Annual geographical distributions illustrating the assessment of MERRA-2 dust-to-total AOD ratio versus
1841 CALIOP retrievals, during daytime conditions at $1^\circ \times 1^\circ$ spatial resolution, according to the primary skill metrics of: (i)
1842 mean bias, (ii) fractional bias, (iii) fractional gross error and (iv) correlation coefficient, representative for the period
1843 2007-2015.
1844
1845



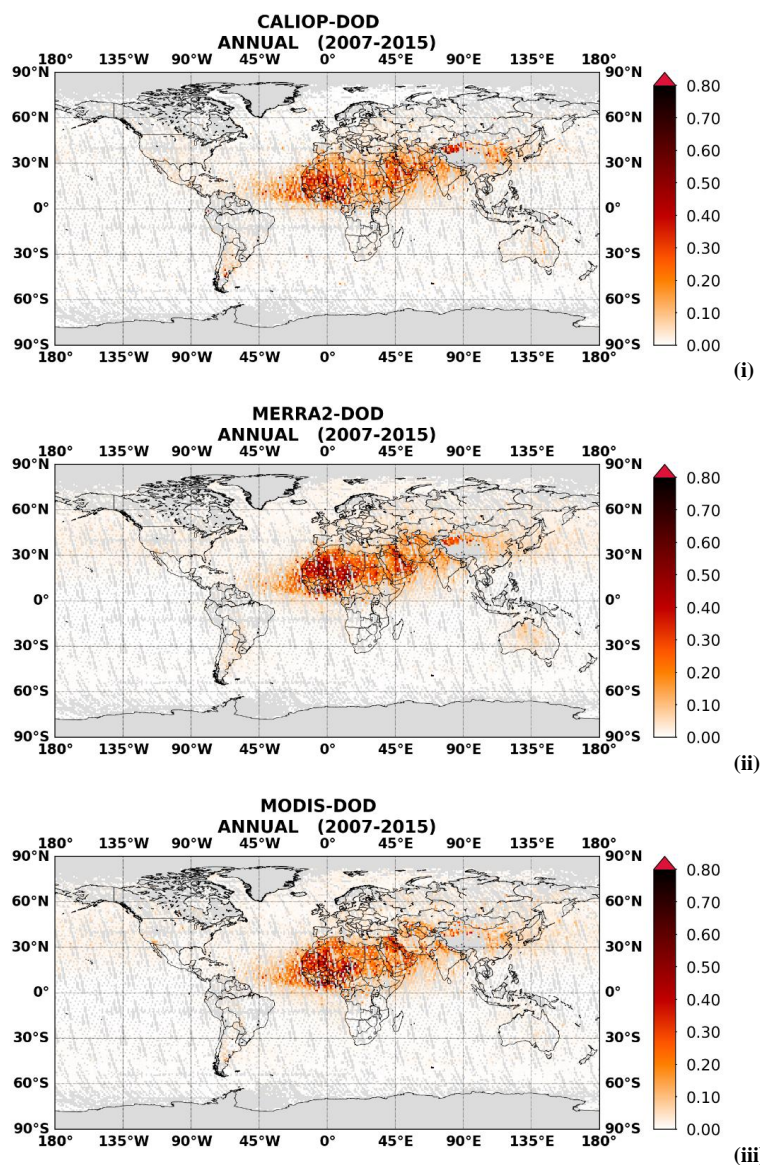
1846 **Figure 4:** (i) AERONET sites where at least one pair of ground-based and spaceborne retrievals has been recorded,
1847 according to the defined collocation criteria, during the period 2007 – 2016. (ii) Density scatterplot between MODIS (y-
1848 axis) and AERONET (x-axis) dust optical depth at 550nm. The solid and dashed lines stand for the linear regression fit
1849 and equal line ($y=x$), respectively. LOC in the titles indicates that both land (L) and ocean (OC) MODIS retrievals are
1850 considered.

1851
1852
1853
1854
1855
1856
1857
1858
1859
1860
1861



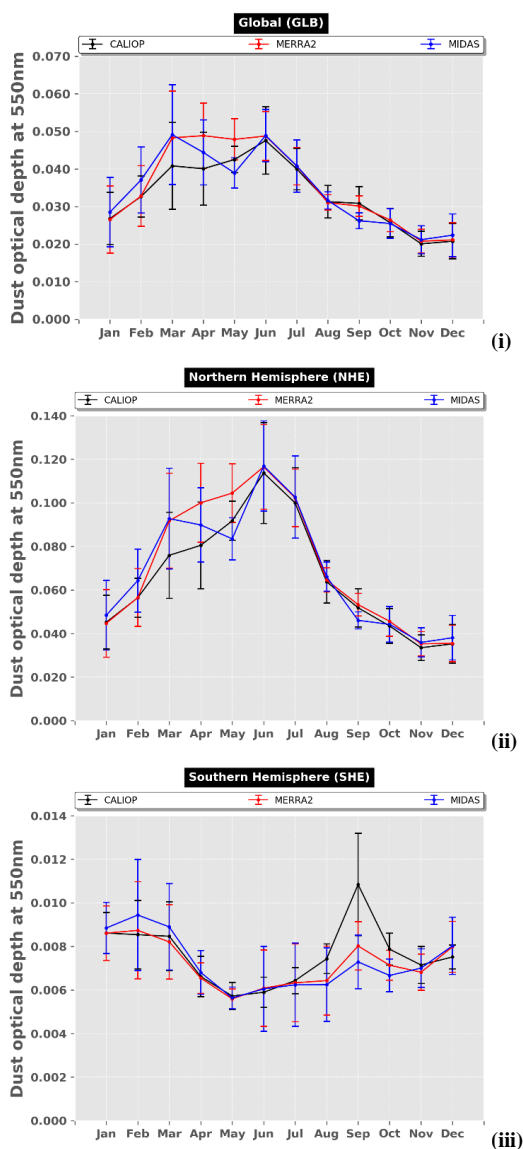
1862 **Figure 5:** Scatterplot metrics between MODIS and AERONET DOD_{550nm}, at station level, during the period 2007 – 2016.
1863 (i) Number of concurrent MODIS-AERONET observations, (ii) correlation coefficient, (iii) root mean square error and
1864 (iv) bias defined as spaceborne minus ground-based retrievals. The obtained scores are presented for sites with at least 30
1865 MODIS-AERONET matchups.

1866
1867
1868
1869
1870
1871
1872
1873
1874
1875
1876
1877
1878
1879
1880
1881
1882
1883
1884
1885
1886
1887
1888



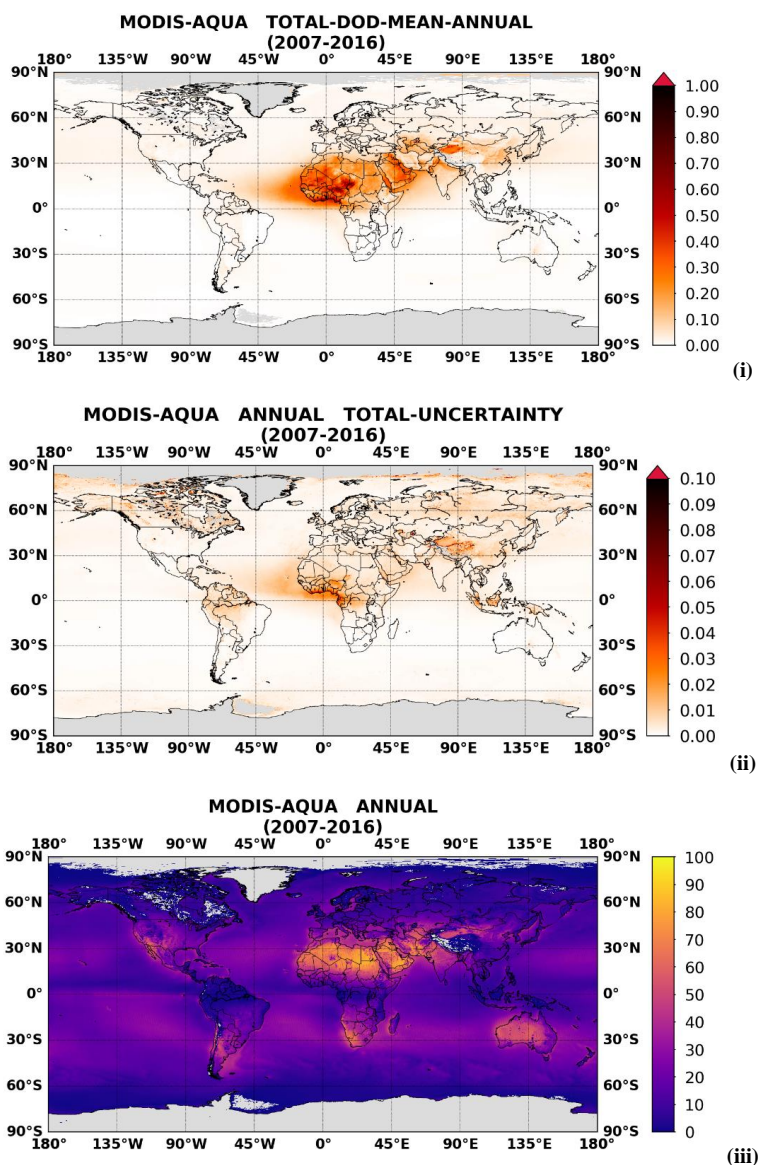
1889 **Figure 6:** Long-term (2007 – 2015) average geographical distributions, at 1° x 1° spatial resolution, of daytime: (i)
1890 CALIOP DOD_{532nm}, (ii) MERRA-2 DOD_{550nm} and (iii) MIDAS (MODIS) DOD_{550nm}.

1891
1892
1893
1894
1895
1896
1897
1898



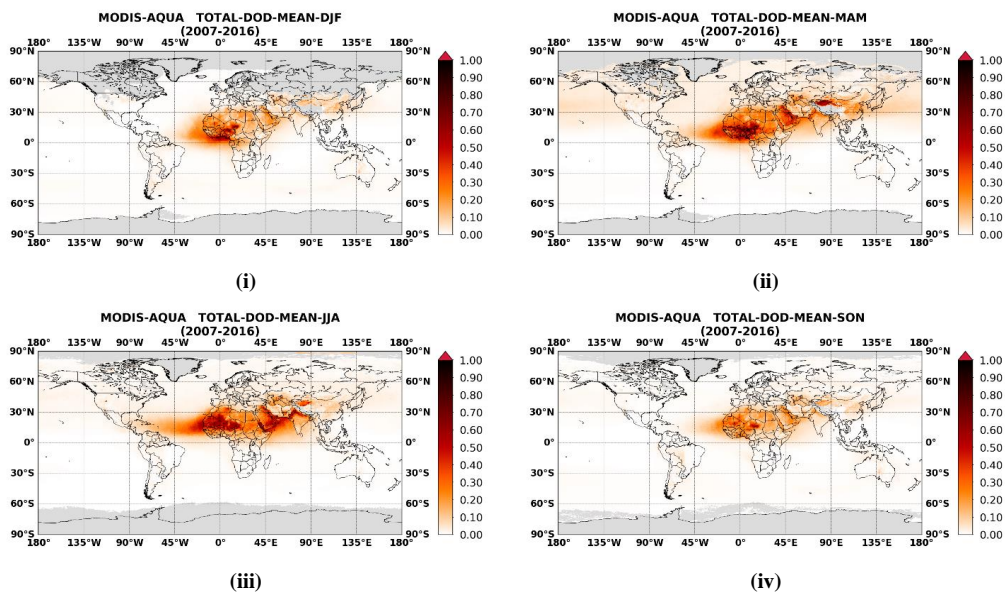
1899 **Figure 7:** Intra-annual variability of CALIOP (black curve), MERRA-2 (red curve) and MODIS (blue curve) monthly
1900 DODs, regionally averaged over: (i) the whole globe (GLB), (ii) the Northern Hemisphere (NHE) and (iii) the Southern
1901 Hemisphere (SHE). The error bars correspond to the standard deviation computed from the interannual timeseries during
1902 the period 2007 – 2015.

1903
1904



1905 **Figure 8:** Annual geographical distributions, at $0.1^\circ \times 0.1^\circ$ spatial resolution, of: (i) the climatological DODs, (ii) the
1906 absolute DOD uncertainty and (iii) the percentage availability of MODIS-Aqua retrievals with respect to the entire study
1907 period spanning from 1 January 2007 to 31 December 2016. Grey color represent areas with absence of data.

1908
1909
1910
1911
1912
1913
1914



1915 **Figure 9:** As in Figure 8-i but for: (i) December-January-February (DJF), (ii) March-April-May (MAM), (iii) June-July-
1916 August (JJA) and (iv) September-October-November (SON).

1917
1918
1919
1920
1921
1922
1923
1924
1925
1926
1927
1928
1929